NTNU
Norwegian University of
Science and Technology

Slip Casting of Solid State SiC

Oda Marie Ellefsen

Materials Science and Engineering (MTMT)
Submission date: July 2018
Supervisor: Mari-Ann Einarsrud, IMA
Co-supervisor: Kjell Wiik, IMA

Norwegian University of Science and Technology
Department of Materials Science and Engineering

Preface

The work described in this master thesis has been completed at the Norwegian University of Science and Technology (NTNU) in the spring of 2018 as part of an MSc degree in Materials Technology. All the results presented in this report are the outcome of experimental work performed over the course of the semester. The choice of dispersant and pH range was based on the project report "Stabilization of dispersions of carbon additives used for sintering of SiC" completed in the fall of 2017 by the same author.

The project has been a cooperation between NTNU and Saint-Gobain Ceramic Materials AS, based in Lillesand. The materials were provided by Saint-Gobain. All experimental work has been performed at the Department of Materials Science and Engineering (IMA) except sintering of the samples which was done by Senior Researcher Vidar Johannessen at Saint-Gobain in Lillesand. In addition, the thermogravimetric measurements were performed by staff engineer Mikko Erik Vedeler Saraste at IMA.

Abstract

A study of the parameters influencing the rheology of silicon carbide slurries containing boron carbide and carbon sintering additives was done. Carbon black and Novolac were used as carbon additives and their effect on rheology and sintering was compared. The dispersant concentration, pH and solid loading were varied to minimize viscosity and maximise solid loading. Several samples were slip cast and the green body density, fracture surface morphology and thermal behaviour were determined. The samples were densified by pressureless sintering and the density, linear shrinkage, fracture mechanisms and phase composition were ascertained.

The viscosity of SiC slurries with carbon black additives was minimised by the addition of 0.5 wt. % anionic polymeric dispersant and pH adjusted to 9. The solid loading could be increased to 76 wt. %. The highest green body and sintered densities were achieved for 75 wt. % solid loading. The highest sintered density reached was 98 % TD.

The viscosity of SiC slurries with Novolac phenolic resin additives was minimised by the addition of 1.5 wt. % dispersant and the pH adjusted close to 8. The solid loading could be increased to 74 wt. %, though this did not lead to increased density. The highest sintered density attained was 93.5 % TD.

Linear shrinkage was reduced with increased green body density in all the samples. Density gradients were uncovered within the green bodies due to packing differences. The effect of the dissolution of Novolac at high pH was determined to be an important contributing factor to the high viscosity of SiC-Novolac slurries.

Sammendrag

Det ble utført en studie av parameterne som påvirker reologien til silisiumkarbid-slikkere som inneholder borkarbid og karbon tilsetninger. Svart karbon og Novolak ble brukt som karbonkilder og deres oppførsel ble sammenlignet. Konsentrasjonen av dispergent, pH og pulverkonsentrasjon ble variert for å minimere viskositet og maksimere faststoff-konsentrasjon i slikkerne. Flere prøver ble slikkerstøpt og grønnkroppstettheten, morfologi på bruddflaten og vekttap ved høy temperatur ble fastslått. Prøvene ble sintret trykkløst og den sintrede tettheten og lineær krymping ble målt. Bruddflater og fasesammensetning ble også evaluert.

Viskositeten til SiC-slikkere med svart karbon ble minimert ved tilsetning av 0,5 wt. % dispergeringsmiddel og pH 9. Faststoffkonsentrasjonen kunne da økes til 76 wt. %. Høyeste grønnkropp- og sintret tetthet ble oppnådd ved faststoffkonsentrasjon på 75 wt. %. Den høyeste sintrede tettheten som ble oppnådd var på 98 % av teoretisk tetthet.

Viskositeten til SiC-slikkere med Novolak fenol-harpiks ble minimert ved tilsetning av 1,5 wt. % dispergeringsmiddel og pH 8. Faststoffkonsentrasjonen kunne økes til 74 wt. %, men dette førte ikke til økt tetthet i de støpte prøvene. Den høyeste sintrede tettheten som ble oppnådd var på 93,5 %.

Lineær krymping ble redusert med økt grønnkropptetthet i alle prøvene. Tetthetsgradienter ble oppdaget i grønnkroppene som var et resultat av forskjellig pakningstetthet av partiklene. En viktig medvirkende faktor til den høye viskositeten til SiC-Novolak-slikkerne var løsning av Novolak i vandige løsninger med høy pH.

Acknowledgements

I would like to thank the many people who have been involved in this master thesis. Firstly, my main supervisor Mari-Ann Einarsrud and co-supervisor Kjell Wiik, for sharing their knowledge and experience to guide my work and supporting me over the course of the project.

Secondly, I would like to thank Pål Runde and Vidar Johannessen at Saint-Gobain Ceramic Materials AS for the opportunity to work with silicon carbide in cooperation with the industry and including me in such an exciting project. Vidar has been a friendly and enthusiastic advisor, whose experience with slip casting was invaluable.

Finally, I would like to thank Mikko Erik Vedeler Saraste for his help with thermogravimetry, the rest of the technical staff, PhD candidates and other scientific staff in the FACET group and the Department of Materials Science at NTNU who have assisted me in my work and given me helpful advice.

Table of Contents

1 Motivation

1.1 Background

Silicon carbide (SiC) is a material with the potential for a wide variety of advanced applications. Originally used as an abrasive because of its hardness, SiC has since found many different applications such as seal rings, diesel engines, electronic circuitry, industrial heat exchangers, gas turbines, and high-temperature conversion systems. [1-5] A few examples of sintered SiC products are presented in Figure 1-1.

Sintered SiC combines low bulk density (3.21 g/cm^3) with high-temperature strength, wear and oxidation resistance. [6] However, one of the main challenges concerning SiC is the difficulty in manufacturing dense products from the powder.[7] Due to strong covalent bonding, low surface energy and self-diffusion, densification requires very high temperature and pressure to reach fully dense sintered products. [8] Solid state sintered silicon carbide is an approach to densifying SiC using boron and carbon as additives allowing for pressureless sintering. [8] Boron is often added as boron carbide, while carbon can be added as carbon black or by pyrolysis of a phenolic resin.

Figure 1-1 A selection of sintered SiC products [9]

Slip casting of SiC is an interesting approach to consolidation of the powder, offering a greater choice of shapes and applications than for example uniaxial pressing. Slip casting is

also easy and cheap to implement, requiring little and inexpensive equipment. The characteristics of the slip are essential to successful green body preparation. Ideally the slip should have a high solid loading while maintaining a low viscosity and high colloidal stability. The difficulties in engineering an ideal slip are multiplied when considering a complex system such as solid state SiC because of the different additives used and the strict requirements of certain applications for the material.

The challenges with SiC are often attributed to the choice and concentration of the sintering additives [10] or the effect of SiO_2 impurity. [11] There are however additional factors to consider when working with slip casting. The homogeneity of the green body, determined in part by the dispersion of the additives and the viscosity of the slip will impact the green body density. Increasing the green density can in turn decrease the dimensional shrinkage and affect the strength of the final sintered product. Controlling the dispersion behaviour and aggregation of the powder in suspension is therefore instrumental to produce high-reliability and high-performance ceramics.

The complexity of the SiC colloidal system means that little work has been done on the stabilization of the dispersions as a whole. Some work has been done on the stabilization of SiC [12-16], boron carbide [17] and carbon black [18-20] individually. There is currently no work concerning the stabilization of insoluble phenolic resin in aqueous suspension but some work has been done on dispersing a soluble phenol-formaldehyde resin. [21]

1.2 Aim of this work

The aim of this master thesis was to investigate slip casting of solid state SiC in three stages from slip preparation, casting to pressureless sintering. Special attention was paid to reducing the viscosity of the slips by adjusting the dispersant concentration and the pH, and to increasing the solid loading. Slip cast green bodies were studied for density, homogeneity and fracture surface morphology. Once sintered, the density of the samples was measured, and the microstructure and phase composition were studied. In addition, two different carbon sources were used: carbon black and Novolac. The difference between these was also discussed. The goal was to make an in-depth analysis of the parameters influencing slip casting as a green body consolidation method for solid-state SiC and make suggestions for improvements in the process.

2 Introduction

2.1 Silicon carbide

Silicon carbide was first synthesized by American inventor Edward G. Acheson in 1891 in an attempt to produce synthetic diamonds. Acheson's initial method consisted of heating a mixture of clay and powdered coke in an iron bowl. An ordinary carbon arc-light served as the electrodes. The resulting green crystals formed were called carborundum from the naturally occurring alumina compound corundum and Acheson thinking the crystals were a compound of the carbon and the alumina in the clay. The hardness of carborundum was found to approximate the hardness of diamonds and Acheson subsequently applied for a U.S. patent. The original product was offered for polishing gems, then became ubiquitous as an industrial abrasive. [22]

The Acheson process remains the preferred production route for large scale synthesis of SiC. The basic design principles of the furnace have remained unchanged while the furnace size and efficiency have increased. The furnace is either cylindrical or U-shaped with two electrodes connected to a graphite core laid within a surrounding mixture of reactant petroleum coke and silica sand. An electric current is passed through heating the reactants to form SiC and carbon monoxide. The temperature in the core is in the range of 2800-3000 °C and the process usually lasts 45 to 60 hours before cooling. [23] The total reaction is given as

$$SiO_2 + 3\ C \rightarrow SiC + 2\ CO \tag{2.1}$$

though the thermodynamics of the reaction make it highly unlikely as extensive diffusion would be required to bring Si atoms in proximity to C atoms. Instead SiC forms as a result of four sub-reactions providing mass transfer in the vapour phase [23]:

$$C + SiO_2 \rightarrow SiO\ (g) + CO\ (g) \tag{2.2}$$

$$SiO_2 + CO\ (g) \rightarrow SiO + CO_2\ (g) \tag{2.3}$$

$$C + CO_2\ (g) \rightarrow 2\ CO\ (g) \tag{2.4}$$

$$2\ C + SiO \rightarrow SiC + CO\ (g) \tag{2.5}$$

First the SiO_2 particles react with adjacent coke particles liberating SiO and CO gas. The CO reacts with other SiO_2 to form more SiO and CO_2. The CO_2 is reduced by carbon to form CO and the SiO reacts directly with carbon to form SiC and CO gas. The majority of the SiC is formed through these reactions at temperatures above 1970 K (1697 °C) though SiO can react at lower temperatures directly at the surface of carbon particles to form SiC. [23]

2.1.1 Structure

SiC occurs mainly in two different crystal structures: β-SiC with a cubic zinc blende structure and a variety of hexagonal and rhombohedral polytypes called α-SiC. The number of α-SiC polytypes exceed 200 but the most common is the hexagonal wurtzite 6H-SiC. β-SiC has a structure analogous to the diamond structure and is synthesized at temperatures below 2100°C. [24]

The building blocks of SiC crystals are SiC_4 and CSi_4 tetrahedra and the polytypes are a result of different stacking sequences. The 3C and 6H polytypes are presented in Figure 2-1. Ramsdell notation uses a letter for the type of structure (cubic, hexagonal or rhombohedral) and a number for the smallest number of layers in the repeating unit.

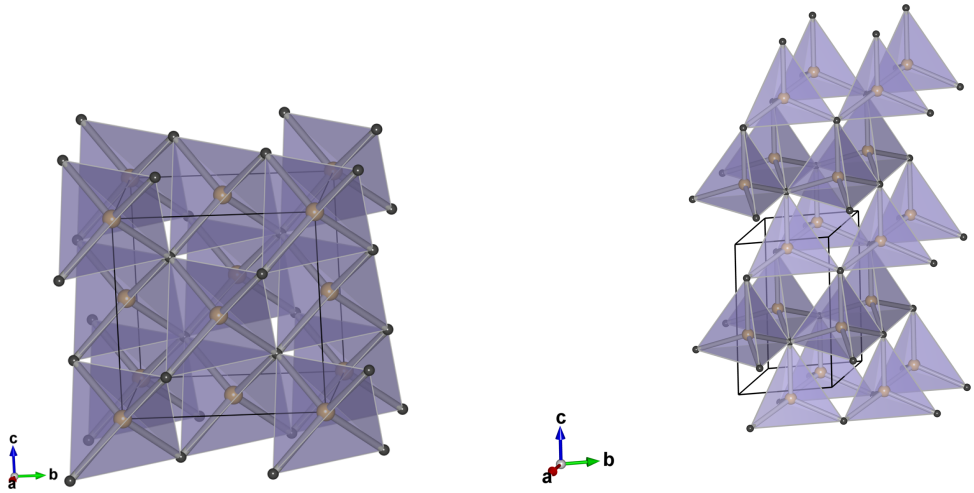

Figure 2-1 Crystal structures of 3C-SiC (left) and 6H-SiC (right). Si and C are the yellow and grey spheres respectively. [25]

2.1.2 Properties and applications

SiC has high hardness compared to most materials, but there are other properties that make it an interesting material for many different applications. Some key properties are low specific density, chemical inertness at high temperatures, low thermal expansion and thermal shock resistance. SiC is also used as a wide band-gap semiconductor at high temperatures. A few properties of SiC are presented in Table 2-1.

Table 2-1 A selection of properties of two common SiC polytypes [24]

Property	**Unit**	**SiC-3C**	**SiC-6H**
Crystal structure	-	Zinc blende (cubic)	Hexagonal
Density	g cm^{-3}	3.21	3.21
E-modulus	GPa	475	-
Thermal conductivity	W m^{-1} K^{-1}	25.5	41
Specific heat	J mol^{-1} K^{-1}	28.63	27.69
Thermal expansion coefficient	10^{-6} K^{-1}	3.8	5.12
Vicker's hardness	GPa	24.5-28.2	-
Flexural strength	MPa	350-600	-

Developments in SiC technology have expanded the originally narrow field of applications as an abrasive to many technologically advanced industries. High temperature components have been developed for aircraft and automotive engine sensors, transmitters for deep well drilling and jet engine ignition systems.[1, 3-5] Furthermore, the high temperature stability and strength makes SiC an interesting replacement for silicon in high temperature, high voltage and high-power semiconductor applications. [2, 24] The wide energy band-gap (3.0-3.2 eV) allows for operation in higher temperatures and radiation levels. [26]

A comparison of commercially available SiC products for kiln furniture has concluded that solid-state sintered SiC has superior qualities for this application. Indeed, solid-state SiC has a higher modulus of rupture (MOR), better oxidation resistance, and higher application temperature than recrystallized, nitride-bonded and reaction sintered SiC. [27]

2.2 Sintering of SiC

Densification of particulate ceramic compacts is a critical step in ceramic processing where the products reach their desired properties. The success of the process is often measured in the achieved density relative to the theoretical density and by the decrease in porosity in the sample. Pores and pore size are factors that will impact the toughness and strength of the final product as they are defects that can lead to failure of the material at a stress much lower than the theoretical fracture stress.

Sintering is characterized by a relative decrease in product size as is required for densification. However, there are mechanisms that lead to coarsening of the grains and grain size increase. These effects need to be avoided as large grains are also detrimental for high strength. In addition, the quality of the final sintered product is highly dependent on the characteristics of the green body and the choices made in powder preparation, consolidation and, finally, sintering conditions.

2.2.1 Driving forces for sintering

The foundation of sintering is the transport of mass between powder particles, initially manifesting as the formation of necks as shown in Figure 2-2. In general, mass transport can occur in the gas phase, liquid phase or solid-state. Reduction in surface free energy, applied pressure or chemical reactions can create a global driving force for mass transport. [28] The simplest form of sintering relies only on the reduction of the surface free energy and is the main driving force in pressureless sintering.

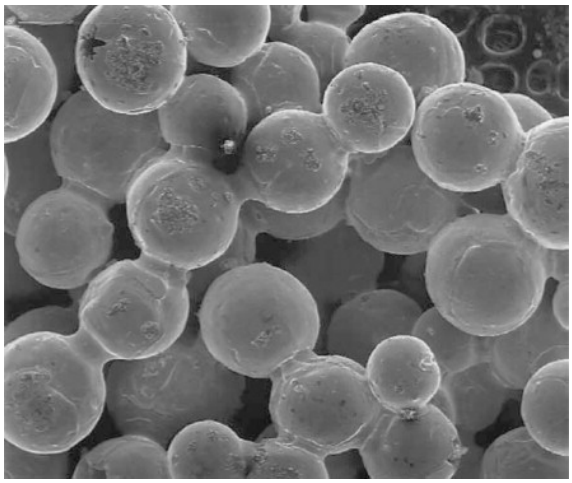

Figure 2-2 SEM image of the neck formed between bronze particles after sintering at 800 °C [29]

Reducing the total surface area or transforming solid-vapour interfaces to solid-solid interfaces can reduce the surface free energy, but only the second process will lead to densification of the solid. Grain boundary energy is generally lower than solid-vapour surface energy so the process is thermodynamically favourable. [29] Reduction in the total surface area will, however, lead to coarsening as large pores and particles grow at the expense of smaller ones. Careful control of the sintering parameters, such as time, temperature, and sintering additives is crucial to favour the densifying process over coarsening.

Transport through the gas phase can occur due to the difference in partial pressure over curved and flat surfaces. This leads to transport from the particle surface to the inter-particle necks and no change in inter-particle distance. This process is illustrated in Figure 2-3. The partial pressure is higher over a concave surface and so, given sufficient energy and time, atoms will move from the convex to the concave surface, resulting in a flat surface. [30]

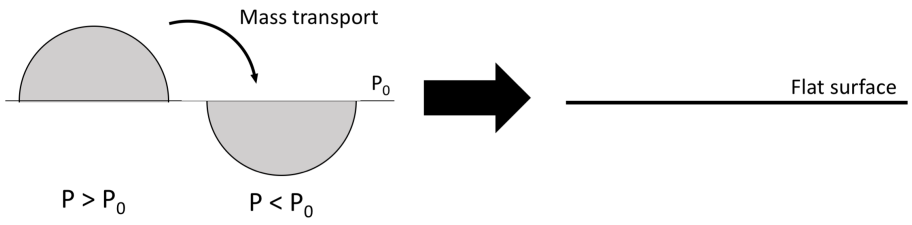

Figure 2-3 Mass transport occurs from a convex to a concave surface due to the differences in partial pressure over the surfaces. This leads to a flat surface given sufficient energy and time.

On the other hand, atoms can diffuse from the bulk to the surface as long as there are a sufficient number of vacancies. Solid state diffusion is driven by the concentration gradient of vacancies that occurs due to differences in surface curvature. [30] The number of vacancies is higher for a concave than for a convex surface, so atoms are encouraged to diffuse towards the concave surface. Encouraging diffusion from the bulk to the neck will allow for densification. The different transport mechanisms available in polycrystalline ceramics are outlined in the next section.

2.2.2 Mass transport mechanisms for sintering polycrystalline ceramics

Sintering theory dictates that the reduction in free energy is dependent on the five mass transport mechanisms listed in Table 2-2 and presented in Figure 2-4. For densification to occur, atoms must be transported from the bulk material to the neck. Surface transport will only yield neck growth without change in inter-particle spacing. [29]

Table 2-2 Mass transport paths in solid-state sintering and their effect [31]

Mass transport mechanism	**Effect**
Evaporation-condensation	Coarsening
Surface diffusion	Coarsening
Lattice diffusion from the surface	Coarsening
Lattice diffusion form the grain boundaries	Densifying
Grain boundary diffusion	Densifying

The densification mechanisms in polycrystalline ceramics are lattice diffusion from the grain boundary and grain boundary diffusion. Surface diffusion, lattice diffusion from the surface and evaporation-condensation are coarsening mechanisms which change the pore shape by neck size growth. These non-densifying mechanisms are important as they will reduce the rate of the densifying mechanisms. [31]

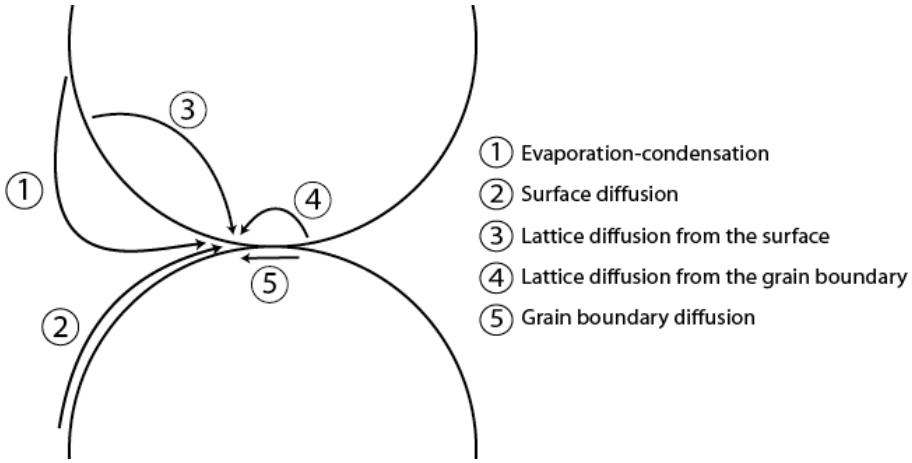

Figure 2-4 Mass transport mechanisms for solid-state sintering. Mechanisms 1-3 are coarsening while 4 and 5 are densifying. [31]

2.2.3 Sintering stages

The sintering process is often separated into three stages where different processes occur. The initial stage is characterised by the rearrangement of particles and neck formation at the contact points between the particles. This stage involves < 5 % densification. During the intermediate stage, the compact can reach up to 92 % of theoretical density, as the necks grow. The final stage includes the final densification with pore closure and grain growth.

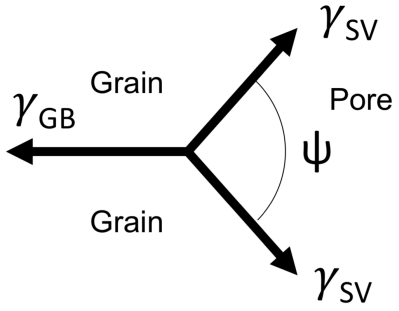

Figure 2-5 The dihedral angle is the angle formed by a grain boundary where it intersects with another solid or pore.

$$\gamma_{GB} = 2\gamma_{SV}\cos\left(\frac{\Psi}{2}\right) \tag{2.6}$$

Removal of pores during the intermediate stage is related to the pore shape. The dihedral angle describes the angle between grains as seen in Figure 2-5. A necessary condition for sintering is that the grain boundary energy (γ_{GB}) is lower than twice the solid-vapour surface

energy (γ_{SV}). Given equation (2.6), this means that the dihedral angle needs to be < 180° for sintering to occur. [29]

2.2.4 Solid-state sintered SiC

The strong covalent bonding in SiC is a fundamental characteristic for many of the properties discussed in section 2.1.2. It is however also an important impediment to sintering, making SiC difficult to sinter using traditional methods because the thermodynamic driving forces are too weak for mass transport to occur. In response to this, several approaches have been developed. Sintering with applied pressure, like hot-pressing or spark plasma sintering, are common though require special equipment. The additional energy provided by the externally applied pressure increases the driving forces for the system to lower its free energy. [28] Another option is using additives to increase the driving forces and allow for pressureless sintering.

For SiC, additives are divided into liquid phase and solid state, depending on the type of sintering mechanisms that are desired. In this master thesis, solid-state sintering has been the focus. Boron in the form of B_4C and carbon are used to create driving forces for the diffusional mass transport for densification. [8] Carbon can be added in the form of carbon black or as a phenolic resin that will pyrolyse to form pure carbon during sintering in inert atmospheres.

Pressureless sintering of SiC was first performed by Prochazka [32] via solid-state sintering using boron and carbon as additives. However, to reach high sintered density (above 95 % of theoretical density) sintering temperatures above 2100 °C are required which can lead to exaggerated grain growth.

The addition of carbon was initially thought to only reduce the surface energy and promote the sintering of boron doped SiC. At temperatures above 1520 °C the assumption is that carbon will remove the surface silica by the following reaction [7]:

$$SiO_2\,(s) + 3\,C\,(s) \rightarrow SiC\,(s) + 2\,CO\,(g) \qquad (2.7)$$

There are, however, other mechanisms that can remove the surface silica during sintering. SiO_2 can be reduced by itself in the absence of carbon above 1870 °C following the reaction:

$$2\ SiO_2\ (s) + SiC\ (s) \rightarrow 3\ SiO\ (g) + CO\ (g) \quad (2.8)$$

Silicon deposition can also be a transport mechanism above 1950 °C:

$$SiO\ (g) + SiC\ (s) \rightarrow 2\ Si\ (l) + CO\ (g) \quad (2.9)$$

The formation of volatile SiO would promote vapour phase transport which inhibits densification and leads to coarsening. The presence of gas also leads to a network of pores that cannot be removed by heat treatment. [33]

Another role of carbon for densification of SiC has been proposed. Datta et al. suggested the presence of carbon creates an excess carbon partial pressure that decreases carbon vacancies and promoted silicon vacancies. This increases the diffusion coefficient of silicon and decreases that of carbon, thereby increasing the bulk diffusion of SiC. [10]

The mechanism of boron is more debated, though there is definite agreement that boron additives will increase the density. The first explanation, suggested by Prochazka, was that boron segregates to the grain boundaries and decreases the grain boundary to surface energy ratio, thereby increasing the driving force for densification. However, Greskovich and Rosolowski showed that both densifying and non-densifying powders had dihedral angles ≥ 100 °, which indicates that densification is not limited by energy considerations. [34] Clegg suggested that boron increases the grain boundary diffusion coefficient. [33] Gross et al. considered that boron could increase bulk or grain boundary diffusion rates or inhibit the surface diffusion and evaporation-condensation. [35]

Datta et al. reported the sintering temperature for solid-state sintering of α-SiC can be as low as 2050 °C with the addition of 0.5 wt. % B_4C and 1 wt. % C, reaching a relative density of 99 %. [10] Even lower sintering temperatures have been achieved by Magnani et al. by using a two-step sintering process. [36]

2.3 Green body consolidation by slip casting

Ceramics require different forming methods than those commonly used for other materials. Silicon carbide is too brittle to be deformed like metals and it will decompose before melting, so fusion casting is not possible. [30] Therefore, most ceramics like SiC, are formed by

powder processing and consolidation prior to sintering. There are several possible approaches to this step, though dry pressing and slip casting are most common.

Slip casting is a colloidal method for consolidation that has been used in traditional ceramics for mass production of pottery, porcelain and other traditional ceramics. The technique is well suited for intricate designs and thin walls and one notable example is sanitary ware such as toilet bowls and basins as seen in Figure 2-6. The technique can also be applied to technologically advanced ceramic production with many of the same benefits.

Figure 2-6 Demoulding of slip casted sanitary ware in a Roca factory [37]

The method consists of dispersing a ceramic powder in a liquid medium, commonly water, to form a slip. The slip is poured into a plaster mould and the liquid medium is removed by capillary forces in the mould, inducing a controlled settling of the solid particles. The particles are thereby brought closer together allowing inter-particle attraction to function more strongly. [30] Figure 2-2 shows the steps of the slip casting process from slip to green body.

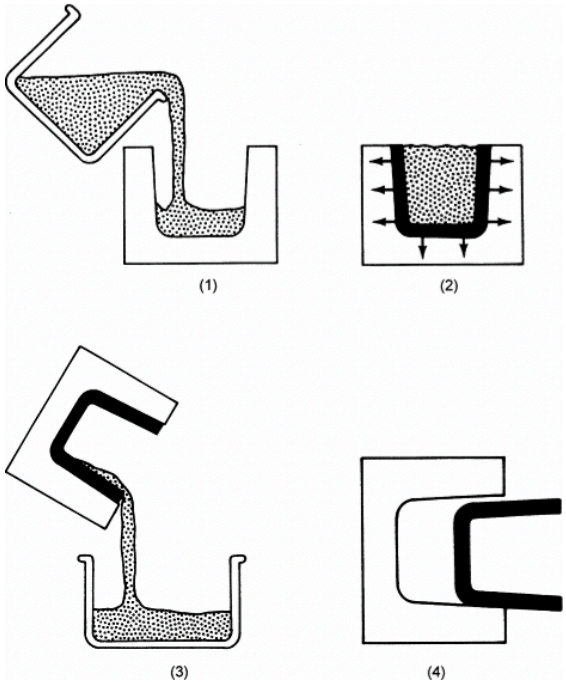

Figure 2-7 The steps of the slip casting process: (1) casting the slip, (2) formation of a solid by controlled settling, (3) removal of excess slip and (4) demoulding. [30]

The casting properties of the slip are mostly dependent on its dispersion and viscosity. The ideal slip is completely deflocculated, has a low viscosity and thixotropy while having a high percentage of solid particles relative to the liquid phase. [38] These properties can be achieved by controlling the surface charges developed on the particles when immersed in the liquid medium, measured by the zeta potential as a function of pH. Increasing the solid loading further can be achieved by using dispersing or deflocculating agents that introduce larger energy barriers against flocculation thereby increasing the stability of the dispersion.

Particle size distribution is also important, and the casting properties have been found to be largely dependent on the manner of distribution of particles between the upper and lower size limit. [30] Typically the packing of monodisperse hard spheres is limited by random close packing (RPC) of ~0.64 while a non-homogeneous distribution of sizes increases the overall dense packing fraction of the system. [39] It follows that the particle size distribution should ideally approach an optimum packing structure though, particles can often not be simplified as perfect spheres, leading to deviation from these theoretical values.

2.3.1 Colloidal theory for ceramic processing

As mentioned previously, a major requirement for slip casting is that the solid is well dispersed in the liquid and the flow of the slurry is sufficient to properly fill the mould. In addition, for complex systems containing several different particle compositions, the homogeneity of the suspension has to be insured. Colloidal stability of solid particles is determined by the surface properties of the particles and the liquid medium. All particles will acquire a surface charge when submerged in a polar liquid medium such as water. For metal oxides and materials that contain carboxylic acid and amine-type functional groups, the ionization of the surface groups is the main charging mechanism. Furthermore, particles will form a solvated layer that is influenced by the solution conditions.

The Derjaguin-Landau-Verwey-Overbeek (DLVO) theory of colloids is used to describe the aggregation of aqueous dispersions by describing the forces between charged particle surfaces. [40] The theory combines the effect of van der Waals forces, electrostatic repulsion and the Born repulsive forces.[40] The sum of the attractive and repulsive forces gives the net interaction energy:

$$\phi_{net} = 64 k_B T n_\infty \kappa^{-1} \tau_o^2 \exp(-\kappa d) - \left(\frac{A}{12\pi}\right) d^{-2} \tag{2.10}$$

k_B: Boltzmann constant
T: temperature
n_∞: Bulk concentration
$1/\kappa$: Debye length
τ_o: Gouy-Chapman surface potential
A: Hamaker constant
d: distance from surface

Φ_{net} as a function of separation distance between particles is presented in Figure 2-8. The attractive energy is due to the Van der Waals forces. These are relatively long range and characterised by the Hamaker constant (A) of the material. Very close to the surface the Born repulsive forces dominate though these are short-ranged and do not provide any repulsion in the dispersion. The electrostatic repulsion depends on the surface potential of the particles and the solution conditions, specifically the presence of electrolytes and their ionic strength. DLVO theory predicts strong flocculation at the primary minimum while the secondary minimum yields weak flocculation. The difference V_{MAX} between these minima can be

considered the energy barrier against flocculation and is dependent on the effective Hamaker constant, the surface potential and the ionic strength of the electrolyte. [40]

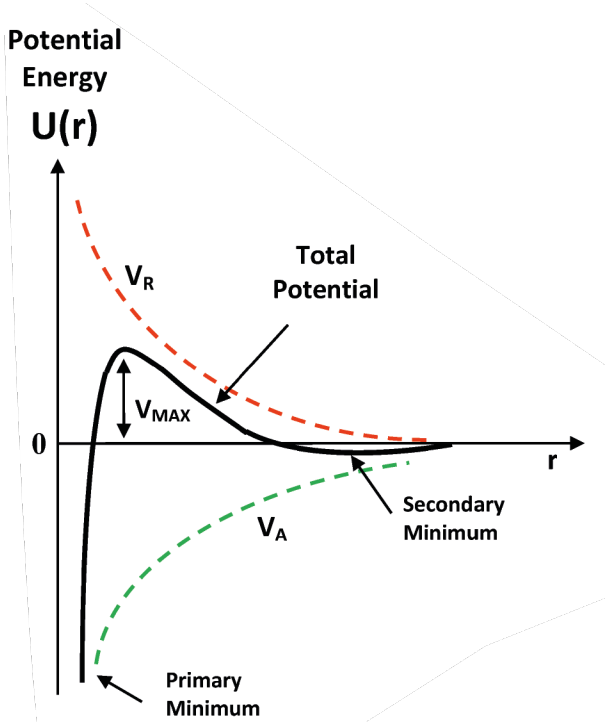

Figure 2-8 The net interaction energy between particles (black line) is the sum of the attractive (green line) and repulsive (red line) interactions. Modified from [41]

The variation in the ion density and surface charge near interfaces of solvated particles is called the electric double layer (EDL). The layer is developed in order to neutralize surface charges developed on particles. Several models are used to describe the electrical potential variation near a charged surface, generated by the ion distribution. The simplest model is the capacitor model which considers only the electrostatic interactions and not the temperature effects, so the potential decreases linearly from the surface to the bulk fluid. [40] This model is especially ill suited for systems where one phase is an aqueous electrolyte because the distribution of counter-ions changes with the distance from the surface.

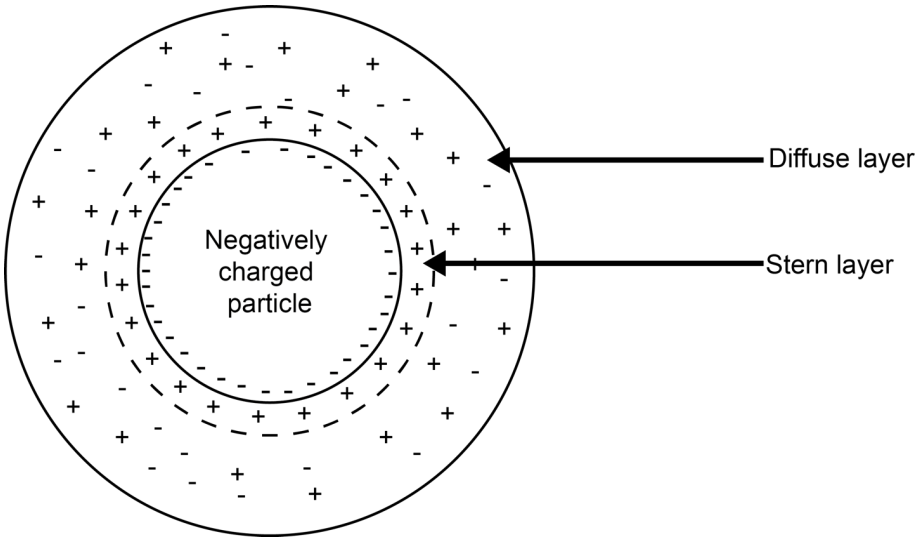

Figure 2-9 The layers surrounding a particle in the diffuse layer model. The inner Stern layer contains the ions adsorbed directly onto the particle surface. The outer diffuse layer contains a concentration gradient of ions. [40]

A more appropriate model is the diffuse layer model as presented in Figure 2-9 which describes the electrical potential drop as a function of distance from the particle surface while accounting for the thermal motion of ions. The Stern surface is the hypothetical boundary dividing the double layer surrounding the particle into the ions assumed to be adsorbed on the charged wall and the diffuse part of the ionic cloud called the diffuse layer.

When assuming low potential the general solution of the model can be simplified using the Debye-Hückel approximation given by equation (2.11) for a planar surface [40]

$$\psi = \psi_o e^{-\kappa x} \tag{2.11}$$

where ψ_o is the surface potential, κ is the Debye-Hückel parameter, and x is the distance from the surface. κ is dependent on the ionic strength of the electrolyte determined by its concentration and the oxidation number of the ions. The Debye length, $\lambda = 1/\kappa$, gives an indication of the extension of the double layer. Figure 2-10 shows the fraction of double layer potential versus distance from a surface for different electrolyte conditions calculated with equation (2.11). The extension of the double layer is decreased by increasing the ionic strength.

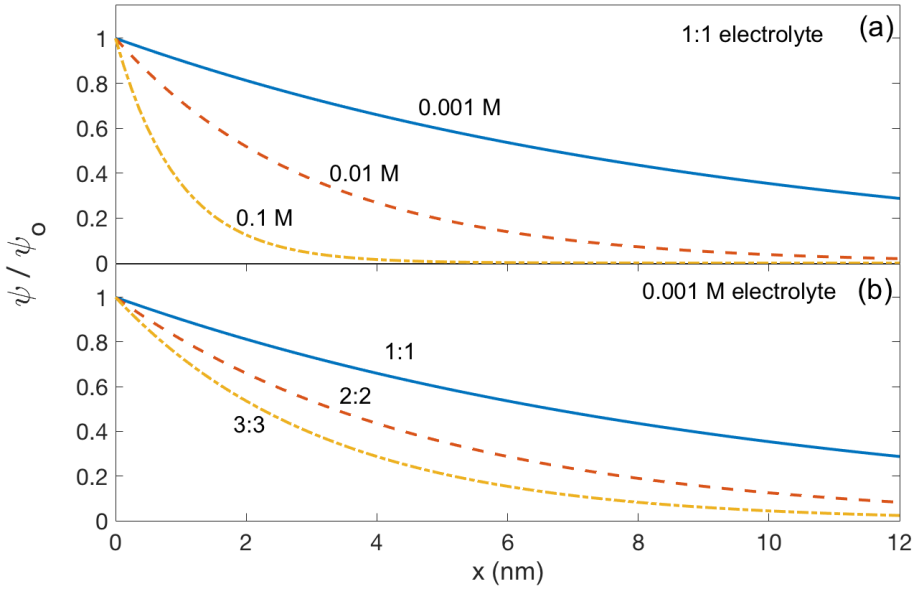

Figure 2-10 Double layer potential as function of distance from the surface for: (a) different concentrations of a 1:1 electrolyte and (b) electrolytes with different oxidation numbers (Z:Z) with a concentration of 10^{-3}M [40]

2.3.2 Dispersion for slip casting of SiC with solid-state sintering aids

The behaviour of the different particles in the solid-state SiC system will vary depending on the surface properties of the particle and the dispersion conditions used. Studies concerning stabilization of certain components of the system in aqueous solutions have been reported most notably on SiC, B_4C and carbon black. No studies have been done regarding the dispersion of insoluble phenolic resins.

Surface properties of SiC and B_4C

SiC particles are covered by a layer of SiO_2 which in water will yield silanol groups. These functional groups are prone to deprotonation in basic solution giving the surface a net negative charge in these conditions:

$$SiOH + H_2O \rightarrow SiO^- + H_3O^+ \qquad (2.12)$$

Increasing the pH will promote the deprotonation of the SiOH groups, thereby increasing the negative surface charge on the SiC-particles. The isoelectric point has been reported to be pH ≈ 4 for α-SiC and pH ≈ 5.5 for β-SiC. [42] As with SiC, the surface potential of B_4C

particles is in large part determined by the surface oxide. Boron carbide has been found to be stable for pH values in the basic region due to the deprotonation of the surface groups. [43]

Carbon black

Carbon black is the result of incomplete combustion of heavy petroleum products and is used as a filler in rubber products and as a colour pigment. It is primarily composed of elemental carbon and forms aggregates and agglomerates. [44] Producing stable aqueous dispersions of carbon black is difficult because of the non-polarity and hydrophobic character. Figure 2-11 shows some of the possible surface groups on carbon. [45] Carbon black particles carry a variety of surface groups that can be ionized in aqueous media. Xu et al. determined the zeta potential of carbon black to be +29.5 mV in neutral pH water. [46] The different surface groups can either undergo protonation or deprotonation and the net surface charge will be highly dependent on pH.

Li et al. were able to successfully stabilize carbon black in aqueous dispersions by modifying the surface with sodium lignosulphonate, an eletrosteric dispersant. They also determined ball milling as an effective way to ensure the particles were well encapsulated and that longer ball milling times increased the stability. [18] Yasin and Luckman found that carbon black could be dispersed by a specific polypropylene oxide/polyethylene oxide (PPO/PEO) co-polymer dispersant called NPE 1800 and that these dispersions had low viscosities in agreement with theoretical predictions. [47]

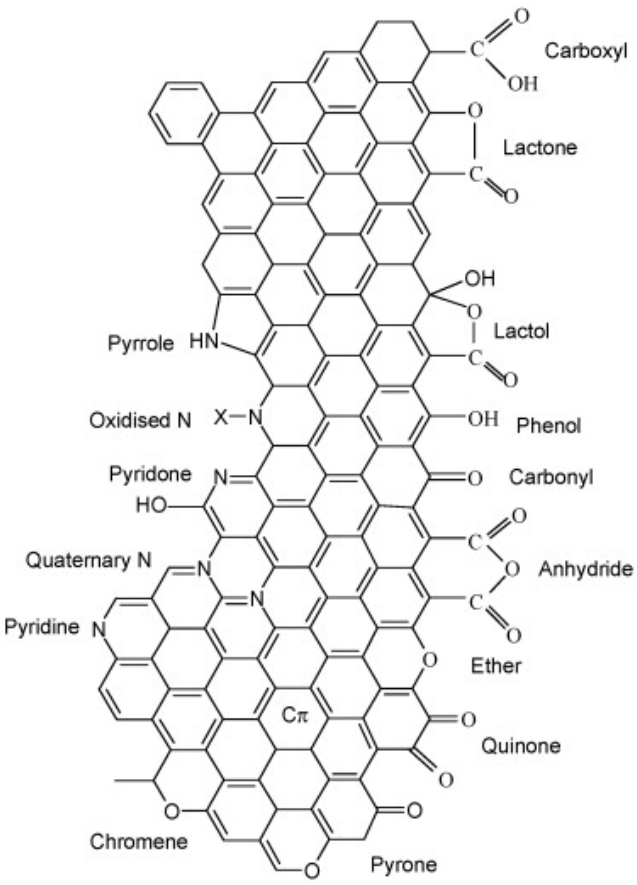

Figure 2-11 Possible surface groups on carbon black particles. [45]

Chemistry of Novolac resins

There are two kinds of resins that are produced by the reaction between phenol and formaldehyde. The first type of resins is called resols and they are produced using a base catalyst and excess formaldehyde. The other type is called Novolacs and they are produced using an acid catalyst and excess phenol. [48] The main difference between these types of phenolic resins is that Novolacs require a curing agent while resols do not. [49]

The molecular structure of Novolac is given in Figure 2-12. It is a linear polymer consisting of phenol groups connected by methylene bridges. The orientation of the phenolic aromatic rings can vary between ortho and para positions and can be controlled by the catalyst used. The number average molecular weight (M_n) of a standard Novolac resin is between 250 and 900. [49]

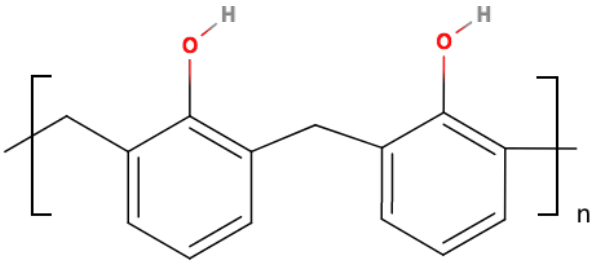

Figure 2-12 Molecular structure of Novolac in ortho-ortho position. [49]

Novolac is chemically stable and insoluble in water under standard conditions. However, one application of Novolac is as a lithographic resist in microlithography and for this application an important parameter is the dissolution of the resist by exposing it to a basic solution called the developer. The dissolution of Novolac is controlled by the deprotonation of the phenol groups following the reaction

$$POH + OH^- \leftrightarrow PO^- + H_2O \tag{2.13}$$

which can be broken down into two steps: the dissociation of the phenolic hydroxide group

$$POH \leftrightarrow PO^- + H^+ \tag{2.14}$$

and the neutralization of the proton by a base

$$H^+ + OH^- \leftrightarrow H_2O \tag{2.15}$$

This deprotonation leads to a negative surface charge on the particles in basic conditions but also the formation of a solved layer on the surface. In addition, several studies have noted the dissolution of Novolac leads to the formation of phenolic strings. These are a result of the polarization of the phenol making it a better hydrogen acceptor because the oxygen atom carries a larger than normal partial negative charge. The phenol can than attract another hydroxyl group that is thereby polarized, forming a string of hydrogen-bonded OH groups. The phenolic strings have been noted to increase the viscosity. [50, 51]

Dispersing agents and stabilization mechanisms

Dispersing agents are an important part of many colloidal dispersions. As mentioned previously, the surface charges can create an electrostatic force when the EDL of two

particles overlap. This force can be repulsive and sufficient to counteract the attractive van der Waals force inducing electrostatic stability. Electrostatic dispersants are molecules that can adsorb on the particle surface and increase the extent of the EDL. In practice, these are effective in low concentration dispersions and in aqueous media. [40]

There are cases when electrostatic stability is not convenient or sufficiently effective. In such cases, polymer-induced colloid stability is an option. Steric dispersants are polymers that adsorb or graft on the particle surface and mask the attractive forces and in some cases provide a repulsive force as well. If the added polymers are polyelectrolytes, then electrostatic and steric effects are combined to create electrosteric stabilization. [30, 40]

The stability of a dispersion is affected by the concentration of steric dispersant because the surface of the particles needs to be sufficiently covered to induce repulsive forces. Stability is achieved at medium concentration through steric stabilization or in some cases at high concentration through depletion stabilization. Figure 2-13 is a simple representation of some of the effects of polymers on dispersion stability.

The repulsive forces arising due to polymers can depend on the density of surface coverage, whether the polymer is grafted or adsorbed on the surface and the quality of the solvent. In the absence of any other forces, the repulsive force is a result of a loss in entropy because the presence of the molecules on the surface restricts the orientational freedom. However, the effects of attraction between polymer segments and interactions with the solvent make it very difficult to predict the behaviour of the dispersant and create a full model. [40]

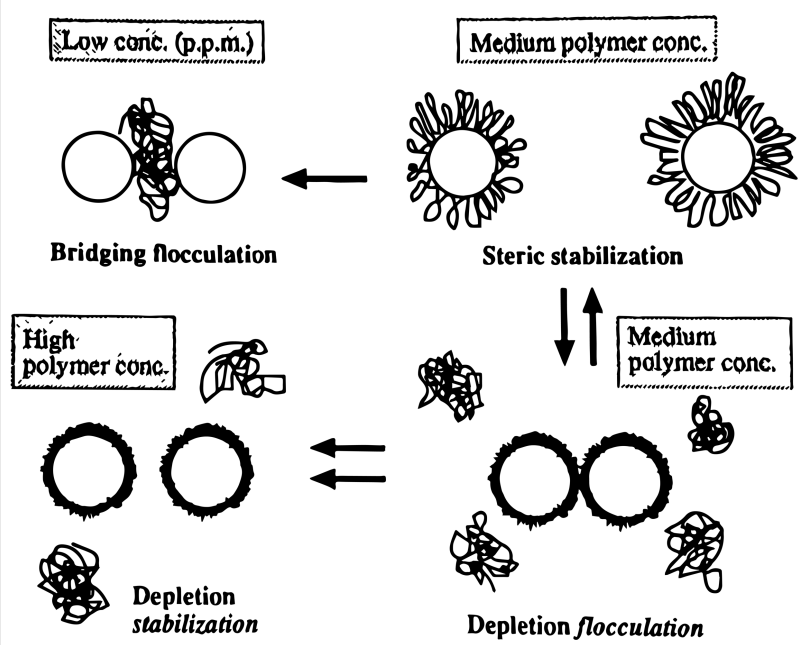

Figure 2-13 The effect of polymer additive concentration on the stability of dispersions [40]

In a previous work by the author, suspensions of Novolac and carbon black were studied. The stability of the suspension was determined qualitatively through sedimentation tests and quantitatively through zeta potential measurements. [52] Several dispersants were tested to compare and contrast their effectiveness and conclusions were made concerning the best dispersant choice and the pH necessary for optimal dispersion.

That study showed the stability of both Novolac and carbon black suspensions was improved the most by dispersants with a steric component, notably Vanisperse CB (Borregård AS, Norway), a sodium lignosulfonate salt and Hypermer KD7 (Croda Nordica AS, Sweden), a modified polyester dispersant with anionic properties. [52] The zeta potential measurements revealed that the pH should be adjusted to ~ 9 in order to maximize the negative surface charge on the particles and improve stability. [52]

Explaining the mechanisms of polymeric dispersants is complicated in the case of non-oxide ceramics like SiC because of the complex surface structures of the particles have in suspension. According to Nojiri et al. the SiC surface is partially reacted and oxidized with water forming SiO_2 and hydroxyl groups. [53] Anionic polymeric dispersants have been shown to be effective at reducing the viscosity and disperse agglomerates. The isoelectric point of SiC is pH = 4-6 so the particles are negatively charged under high pH conditions.

[42] The effectiveness of the anionic dispersant can thus not be explained by electrostatic interactions. [53]

Nojiri et al. explained that the polymeric dispersant was absorbed through the hydrophobic group of the molecule since the hydrophilic group and the negative surface would create repulsive electrostatic forces. This mechanism is illustrated in Figure 2-14. [53] The dispersant used in this thesis, Hypermer KD7, is a modified polyester and its effectiveness can thus be explained by the same mechanism.

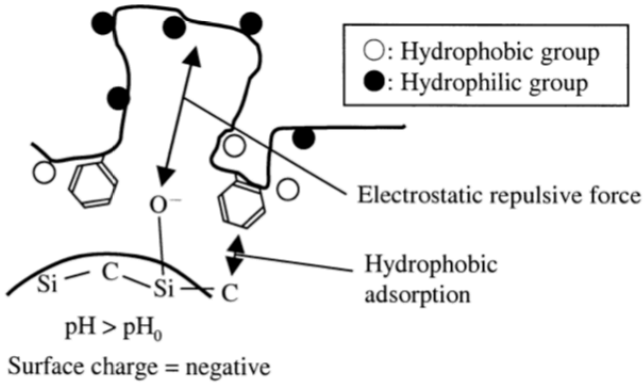

Figure 2-14 Estimated model of anionic polymeric dispersant adsorption mechanism on SiC surface. [53]

2.3.3 Rheology for ceramic slurries

As mentioned in the introduction, the viscosity of ceramic slips is a key property that needs to be controlled. The literature mentions the slip should ideally have a viscosity lower than 100 cP [30] however the rheological behaviour of slurries with high solid loading is complex. The acceptable viscosity for casting can be as a high as 400 cP at a shear rate of 40 s^{-1}.

Rheology is the science of flow and commonly considers a range of parameters. The dynamic or absolute viscosity, η, is defined as a material's resistance to flow. Considering a shear force τ causing a layer of liquid at a distance x from a fixed boundary wall to move with a velocity ν. The viscosity is given by the ratio between the shear force and the shear rate as in equation (2.16) [40]:

$$\eta = \frac{\tau}{\frac{dv}{dx}} = \frac{\tau}{\dot{\gamma}} \tag{2.16}$$

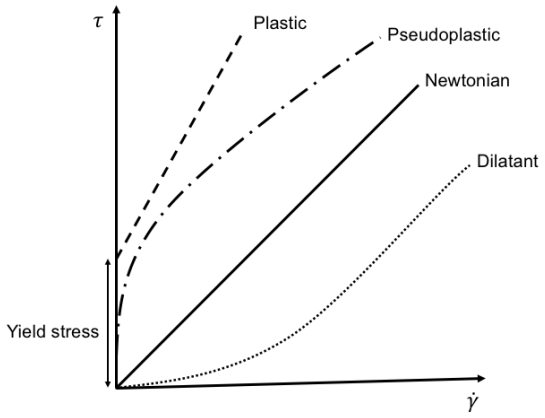

Figure 2-15 Types of flow behaviour represented with shear stress as a function of shear rate. Newtonian flow has constant viscosity for all shear rates. [54]

There are different types of viscous behaviours as shown in Figure 2-15. For Newtonian, or ideal flow, the viscosity is constant and independent of the shear rate. When the viscosity decreases with increasing shear rate the behaviour is called shear-thinning due to plastic (Bingham) or pseudo-plastic behaviour, as is the case with most ceramic slurries. In some cases, the fluid requires a minimum yield stress τ_o in order to flow, in which case the fluid is yield pseudo-plastic. Hence, a single measurement of viscosity is insufficient to properly characterise the flow behaviour. The pseudo-plastic flow of ceramic slurries be modelled using the Herschel-Bulkley model which is given by equation (2.17)

$$\tau = \tau_0 + K\dot{\gamma}^n \tag{2.17}$$

where τ_0 is the yield stress, $\dot{\gamma}$ is the shear rate, K is the consistency index, and n is the flow index. [55] For values of n less than 1 and yield stress larger than 0 the fluid is yield pseudo-plastic. The consistency index is the apparent viscosity for a fixed shear rate and is a proportional constant. The yield stress is the stress required for flow of the suspension and is due to the weakly flocculated particles in the suspension.

The effect of solid concentration on viscosity can be modelled using Einstein's theory on the viscosity of dispersions. The viscosity of a liquid is increased by the addition of particles and dependent on the concentration of particles. However, the theory assumes extremely dilute solutions of rigid spheres with no slippage of the liquid at the surface of the spheres.

Furthermore, it ignores wall effects through certain size restrictions. [56] The equation is given by

$$\frac{\eta}{\eta_0} = 1 + 2.5\,\phi + \cdots \tag{2.18}$$

where η/η_0 is the relative viscosity and ϕ is the volume fraction of particles. The theory will, however, deviate in situations with higher solid loading. Numerous equations have been published in efforts to extend the formula to suspensions of higher concentration. [57, 58] In addition to the volume fraction of particles the viscosity can be influenced by particle size, size distribution, particle shape, chemical conditions such as polymer additives and the slurry temperature. [54]

The Krieger-Dougherty equation, given below, has found widespread application to model concentrated dispersions, though it still assumes spherical monodisperse particles.

$$\frac{\eta}{\eta_0} = (1 - \frac{\phi}{\phi_m})^{-B\phi_m} \tag{2.19}$$

B is the Einstein coefficient (usually 2.5) and ϕ_m is the volume fraction for the densest possible packing. For monodisperse spherical particles $\phi_m \approx 0.74$ at which the viscosity must be infinite. Experimentally, however, the maximum packing is often much lower: $\phi_m \approx 0.64$ in the case of randomly close-packed spheres. [56]

Shear-thinning behaviour, or pseudo-plasticity, is commonly observed in ceramic slurries. It can be considered a special case of thixotropy because the fluid can take a nonzero time to recover the microstructure from prior to shearing. The shear thinning phenomenon is a consequence of the balance between shear conditions the partially aggregated 3D structures that help keep the particles from settling. The possible thixotropic behaviour can be the result of agglomeration formation in the slurry as the shear effectively breaks up these agglomerates the structure of the slurry is broken, and the viscosity decreases. [56]

The rheological properties of a ceramic slurry are dependent on a complex interplay between several interactions [55] :

- Inter-particle attraction promoting the formation of flocs and aggregates
- Hydrodynamic interactions giving rise to viscous dissipation in the liquid

- Frictional interactions created by particle-particle contact

Hydrodynamic interactions are dominant in suspensions with low to medium solid concentration. For these suspensions the viscosity increases linearly with solid loading. Above a certain solid concentration, the viscosity will increase significantly with a small increase in concentration. In this region interactions between particles gain importance and eventually dominate the hydrodynamic effects. Inter-particle attraction is especially significant in suspensions with fine particle sizes and in aqueous suspensions. [55]

Measuring viscosity

Rotational viscometers are common equipment used to determine the flow behaviour of fluids. If we consider a typical concentric cylinder viscometer as shown in Figure 2-16 the shear stress and shear rate are given by equation (2.20) and (2.21) respectively [54].

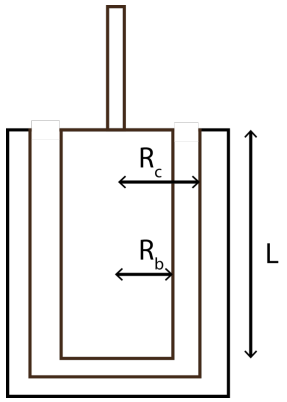

Figure 2-16 Typical concentric cylinder geometry for rheometers with Rb and Rc the radii of the bob and cup respectively and L the length of the bob.

$$\tau = \frac{M}{2\,\pi R_b^2 L} \tag{2.20}$$

$$\dot{\gamma} = \frac{2\,\omega R_c^2}{(R_c^2 - R_b^2)} \tag{2.21}$$

with Rc, the radius of the cup, Rb, the radius of the bob, L, the length of the bob, M the measured torque, and ω, the angular velocity.

Figure 2-17 shows a double gap cylinder type geometry that was used in this study. This geometry maximizes the contact area between the fluid and the bob and therefore allows detection of much smaller torque values. [54]

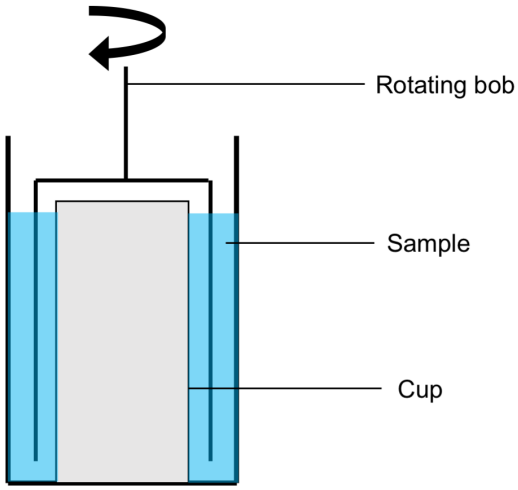

Figure 2-17 Double gap cylinder geometry for rotational viscometers: the surface area between the bob and sample is higher than for traditional cylinder geometries and gives higher accuracy for small torque values. [54]

2.3.4 Review on slip casting of SiC

Several studies have focused on the different parameters that influence slip casting of different ceramics such as slip viscosity, solid loading or particle size, shape and distribution. Ferreira and Diz studied the effect of solids loading and particle shape on the green microstructure of slip cast SiC green bodies. It was determined that the green density could be maximized to reach 74.5 % of the theoretical density by using a 70 wt. % solid loading. Substituting the angular coarse particles that are typical for SiC, with more spherical ones provided an additional increase in green density to 76 % TD. [59]

In addition, Ferreira and Diz showed the solid loading, and by extension, the viscosity of the slip could impact the distribution of the particles in the green bodies. At lower solid contents the fluidity of the slip allowed for segregation between smaller and larger particles leading to an inhomogeneous packing. Increased solid loading reduced, or removed this effect, by increasing the rate of collisions and mutual interference between particles. [59]

The influence of solid loading on the viscosity of slips has been established through the various models of dispersion viscosity mentioned in Section 2.3.3. However, the influence of

solid loading on the packing density and green microstructure of slip cast bodies is still uncertain. A few authors have reported there is no relationship between the solid loading and resulting green density [60-62], while others have observed a linear increase in density [63-65]. Pivinskii and Bevz, as well as, Rutman et al. showed an increase in density up to a certain point before a decrease beyond that concentration of solids. [66, 67]

3 Experimental

3.1 Raw materials

The SiC powders were produced by Saint-Gobain Ceramic Materials AS (Lillesand, Norway) using the Acheson process. The ratio of sintering additives in the two powder batches is presented in Table 3-1. The powder mix batches were produced by Saint-Gobain using co-attrition milling of all the components. The milling, mixing and drying steps were all performed by Saint-Gobain. The specific surface area of the SiC particles was 11-13 m^2/g and the mass median diameter (D_{50}) was 0.90 μm.

Table 3-1 Powder mix composition as received from Saint-Gobain

Name	Carbon source	Carbon [wt. %]	B_4C [wt. %]
SiC-CB	Carbon black	3	1
SiC-Novolac	Novolac resin	7	1

The full list of chemicals used in the experimental work is provided in Table 3-2. The dispersing agent Hypermer KD7 supplied by Croda Nordica AS (Sweden) was used in the slurries. It is a modified polyester with anionic properties. Dolapix A88 (Zschimmer & Schwarz GmbH, Germany) is an aminmethyl propanol that was used as a defoaming agent and partly as a pH adjustor. The pH of the slurries was mainly modified using a dilute solution of ammonia. A liquid PVA, soluble in water, was added to all the slurries as a binder.

Table 3-2 List of chemicals used and their application

Name	Manufacturer	Description and purpose
Hypermer KD7	Croda Nordica AS	Modified polyester with anionic properties for dispersing ceramic powder
Dolapix A88	Zschimmer & Schwarz GmbH	Aminomethyl propanol surfactant used as a defoaming agent and pH adjustor
Binder	Unknown	Liquid PVA in water for binding the green bodies
Ammonia	Sigma Aldrich Norway AS	10 vol. % aqueous ammonia solution for pH adjustment

3.2 Method

An overview of the experimental procedures can be found in Figure 3-1.

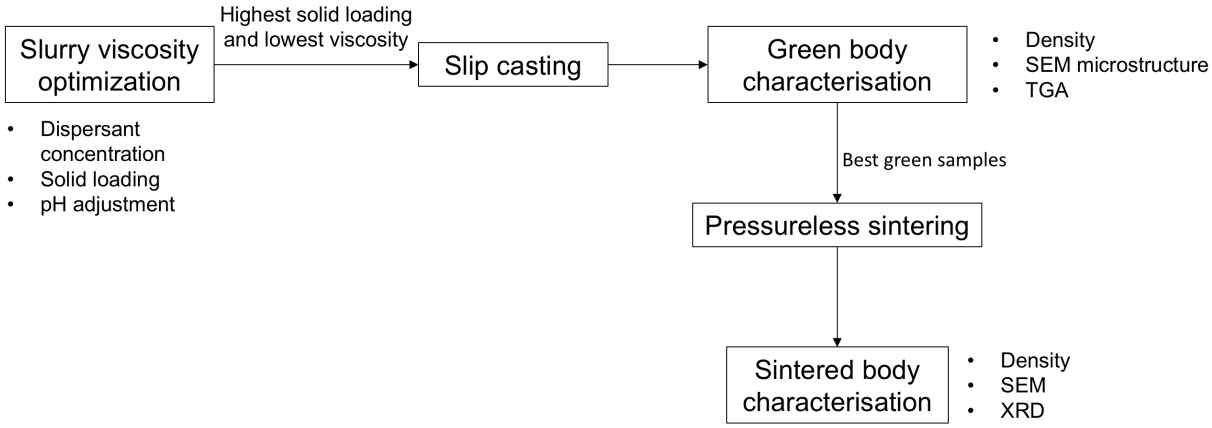

Figure 3-1 Overview of the experimental work presented in this thesis

The sequence of the experimental work was based on the foundations of ceramic engineering. The first step was to optimize the slips by improving the viscosity. The parameters studied were the dispersant concentration and pH. Lowering the viscosity of the slurries allowed an increase in solid loading. The optimal parameters were then implemented in slip casting with

larger scale slurries. The casted bodies could then be analysed with density measurements, SEM of the fracture surfaces and thermal behaviour. Finally, the most promising green bodies were sintered by Saint-Gobain Ceramic Materials AS and the resulting dense bodies could be characterised. The density was measured by the Archimedes method, SEM for the microstructure and X-ray diffraction for the phase composition.

3.2.1 Equipment

The equipment used in the experimental work is listed in Table 3-3.

Table 3-3 List of equipment used and their application

Equipment	Manufacturer and type	Application
Rheometer and measuring systems	Thermo Fischer Haake Mars III with CC27 DG Ti rotor	Slurry viscosity measurement
Scanning electron microscope	Zeiss Supra 55 VP Field-Emission SEM (FE-SEM)	Green body and sintered sample microscopy
Thermal analyser	Netzsch STA 449 C	TGA of Novolac and green bodies
Gold sputter coater	Edwards Sputter Coater S150B	Gold coating green samples for SEM
X-ray diffractometer	Bruker D8 A25 DaVinci	Determine phase composition of raw material and sintered samples
pH meter	Mettler Toledo SevenEasy pH meter S20	Determine pH of slurries
Furnace	Carbolite Gero HTK 8	Sintering of green samples
Polishing machine	Struers TegraPol-31	Sintered sample surface polishing

3.2.2 Rheology measurements

Slurries were prepared for viscosity measurements following the flowchart presented in Figure 3-2. Slurries were mixed in polyethylene bottles with screw caps holding a volume of

250 mL to allow for ball milling. First, the dispersant was added to the water and mixed before the powder was added and the slurry was mixed using a rigid metal spoon. Then the binder was added (5 wt. %), and the pH was adjusted using a diluted ammonia solution. The slurry was mixed by hand to ensure no powder was sticking to the bottom of the container.

Si_3N_4 milling balls were then added and the slurry was ball milled for 2 h at 205 rpm in order to break up any large agglomerates. The milling balls used were spherical, weighed ~ 0.3 g each and were ca. 5 mm in diameter. The milling balls were then removed from the slurry and the viscosity was measured. In some cases, the milling step led to significant foaming so a few drops of Dolapix A88 were added to remove the foam. A list of all the combinations tested is provided in Appendix A Table 9-1.

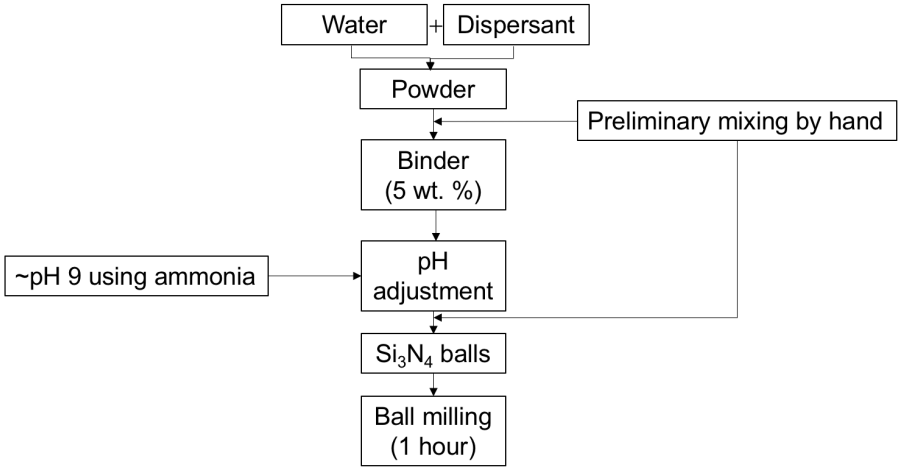

Figure 3-2 Procedure for preparing SiC slurries for viscosity measurement

The rheology of the slurries was determined using a Haake Mars III rheometer with double gap concentric cylinders geometry (CC27 DG Ti rotor). The shear rate was increased from 0 to 100 s^{-1} with a rate of 33 s^{-1}/min, then kept at 100 s^{-1} for 30 s before decreasing to zero at the same rate. The total measurement time was 6.5 min.

3.2.3 Slip casting

The slurries for slip casting were prepared with the same approach as for the viscosity measurements though with a higher volume, using 400 g of powder. The slurries were milled with Si_3N_4 balls (1.5 g each) for 24 h and mixed in polyethylene bottles that could hold 1 L.

After the milling the pH was checked and increased with ammonia solution if it had fallen below 8.7. Dolapix A88 was added dropwise to remove foam.

The active surface of the plaster moulds was prepared by spraying an aqueous suspension of fine talc powder and BN in equal proportions by weight in order to prevent the green bodies from sticking to the moulds. Once the slurry was poured into the cast was left for 24 h, or until dry enough to demould the sample. The samples were dried at 100 °C overnight before weighing and measuring the dimensions.

The plaster moulds used are presented in Figure 3-3 (a). The resulting shape was a rectangular prism with dimensions 180x25x15 mm as presented in Figure 3-3 (b) As is presented in Figure 3-4, the two pieces of the mould were held together using duct tape and a square silicone mould was used as a reservoir to hold excess slip and ensure the moulds were continuously filled as water was drawn out. A plastic lid was placed on top of the silicone container to slow the drying of the surface exposed to air.

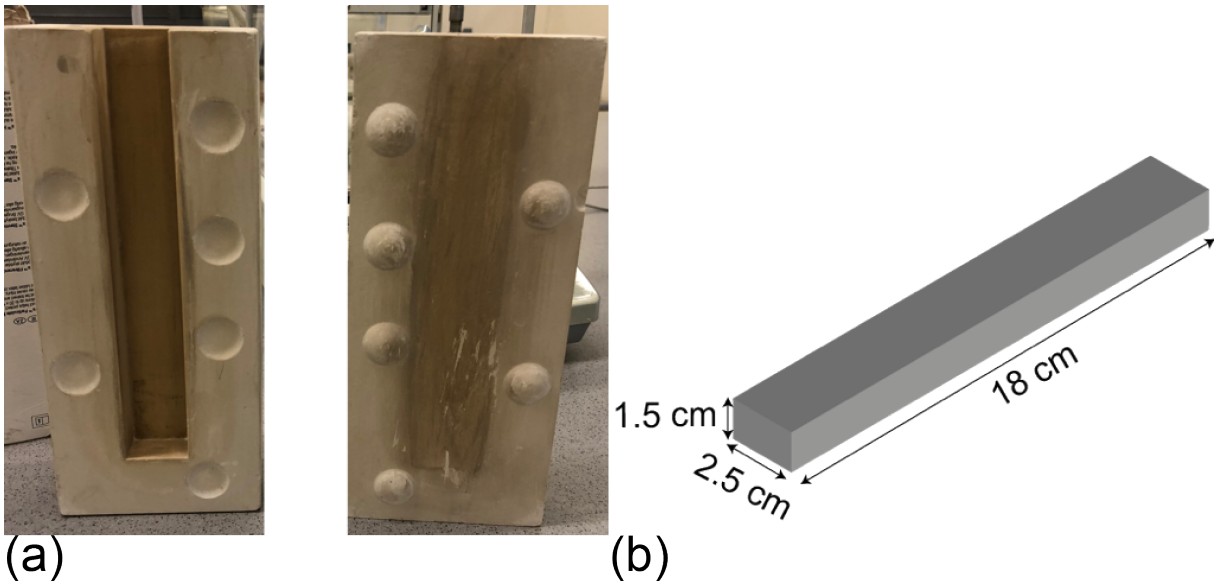

Figure 3-3 (a)Plaster moulds used for slip casting and (b) the resulting shape and dimensions

Figure 3-4 Image of the assembled mould with casted slip. The two mould parts are held together with duct tape and a silicone reservoir (pink) hold the excess slip.

3.2.4 Characterisation of Novolac and green body thermal behaviours

Thermogravimetric analysis was performed using a Netzsch STA 449 C. The thermal decomposition of Novolac was determined in synthetic air and argon gas. The samples, weighing ~ 5 mg, were heated to 1000 °C with a heating rate of 5 °C/min and a dwell time of 200 min at maximum temperature. A gas flow of 30 mL/min was used and the samples were contained in alumina crucibles.

The mass loss of green bodies containing carbon black and Novolac at high temperature in argon was also studied. Green body samples were ground to a powder using an agate mortar and pestle. The powder was sieved to 250 µm. The heating program used is presented in Figure 3-5. The samples were heated in alumina crucibles to 1400 °C with a heating rate of 10 °C/min with a dwell time of 30 min at 120 °C and 4 hours at 1400 °C. The argon gas flow was 30 mL/min.

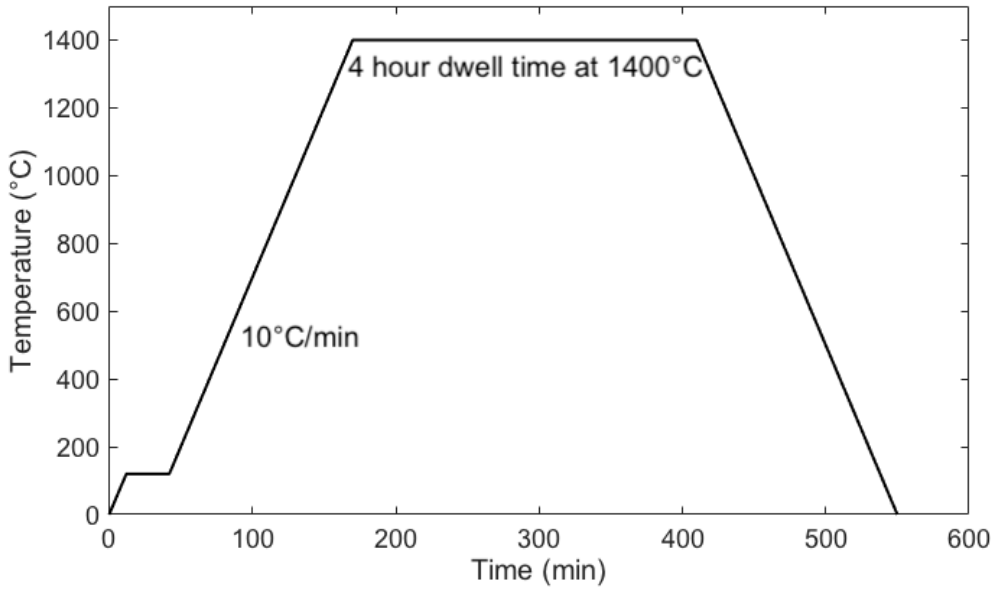

Figure 3-5 Temperature programme used for TGA of green bodies

The fracture surfaces of the green bodies were studied in scanning electron microscope using a Zeiss Supra 55 VP field emission scanning electron microscope (FE-SEM). Secondary electron detection, an electric high tension of 10 kV and a working distance of 9.9 mm and 10.4 mm were used for SiC-CB and SiC-Novolac respectively. The surface of the samples was coated with gold using an Edwards Sputter Coater S150B, to improve conductivity. Images were taken to determine the morphology of the particles, their arrangement in the green body and the overall homogeneity of the sample.

Prior to sintering, the green bodies were cut with a hacksaw or broken into smaller pieces and categorised by their position in the original piece: top, bottom and middle. The green body density was determined geometrically using a digital calliper and a scale. The green body density is given by equation (3.1) where m is the mass of the piece (in g), and l, w and h are the length, width and height of the sample respectively (in cm). The surfaces could be quite uneven, so each measurement was repeated five times and the average was used for the calculation.

$$\rho_{GB} = \frac{m}{l\,w\,h} \tag{3.1}$$

3.2.5 Pressureless sintering

The sintering of the samples was performed by Saint-Gobain Ceramic Materials AS in a Carbolite Gero HTK 8 graphite resistance furnace. The heating programs can be found in Figure 3-6. Prior to sintering samples were heated to 1000 °C for binder burnout. The samples were placed in a graphite box.

The maximum sintering temperature was 2200 °C for the SiC-CB samples and 2150 °C for the SiC-Novolac samples. The dwell time at this temperature was 90 min. The changes in heating and argon rate are important to limit coarsening due to evaporation-condensation mechanisms. The samples were loaded in a graphite box with holes to allow the argon gas to flow. The gas flow was kept at 600 L/h. The atmosphere was enriched with coarse SiC powder.

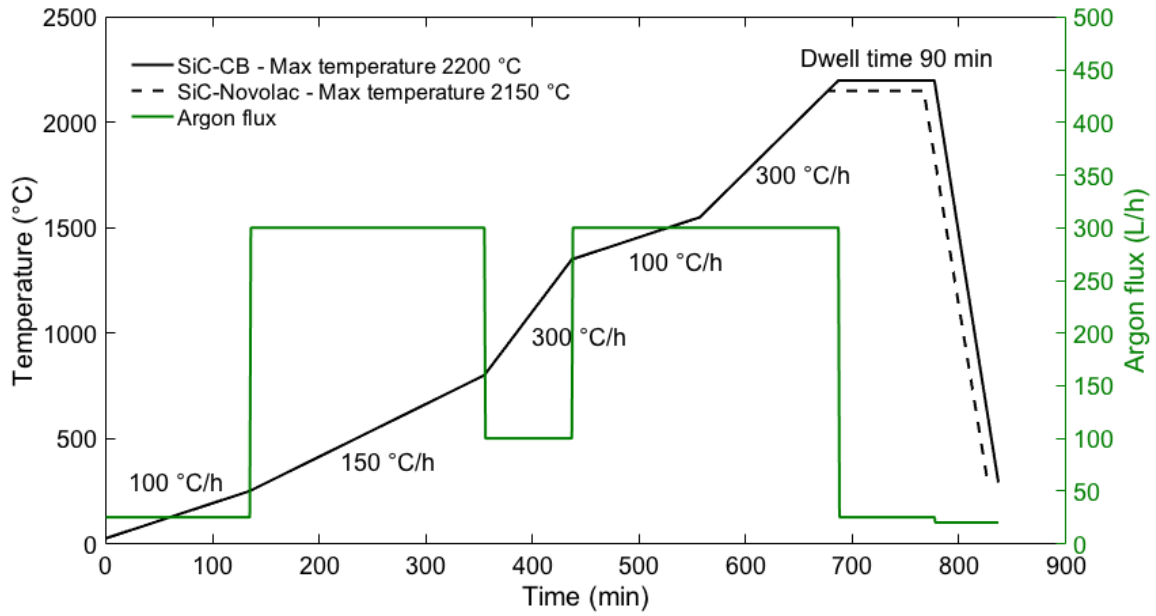

Figure 3-6 Heating program used for pressureless sintering of SiC-CB and SiC-Novolac. The max temperature was 2200 °C for SiC-CB and 2150 °C for SiC-Novolac. The dwell time at max temperature was 90 min.

3.2.6 Characterisation of sintered samples

Density measurement

The bulk densities of the sintered samples were determined using the Archimedes method in a vacuum desiccator. The immersion liquid used was isopropanol. The weight of the dry sample (m_1), immersed (m_2), and wet (m_3) were measured. The equations used for calculating densities are given below.

The density of isopropanol was calculated from equation (3.2):

$$\rho_{liquid} = -0.0009T + 0.8018 \tag{3.2}$$

The bulk density was calculated from equation (3.3):

$$\rho_{bulk} = \frac{m_1}{m_3 - m_2}\rho_{liquid} \tag{3.3}$$

The apparent porosity was determined from equation (3.4):

$$\pi_a = \frac{m_3 - m_1}{m_3 - m_2} * 100 \tag{3.4}$$

The true porosity was calculated with equation (3.5):

$$\pi_t = \frac{\rho_t - \rho_b}{\rho_t} * 100 \tag{3.5}$$

The theoretical density (ρ_{TD}) of the samples was calculated using the rule of mixtures given by equation (3.6), where ρ is the density of the individual components A and B and f is their volume fraction.

$$\rho_{TD} = \rho_A f_A + \rho_B f_B \tag{3.6}$$

It was assumed that the pyrolysis of Novolac during sintering yielded the same composition as SiC-CB in the sintered samples. The theoretical densities of the different components and the computed theoretical density of the products are presented in Table 3-4.

Table 3-4 Theoretical densities of the materials used

Material	Density (g/cm^3)
SiC	3.21
B_4C	2.52
Carbon black*	1.9
Solid-state sintered SiC**	3.1656

* As reported by the manufacturer

** Calculated density

Linear shrinkage

The shrinkage of the samples was calculated using equation (3.7). $L_{sintered}$ and L_o were measured in the height direction as this was the most consistent dimension.

$$\frac{dL}{L_o} = \frac{L_{sintered} - L_o}{L_o} \tag{3.7}$$

Sintered microstructure characterisation

The sintered samples were prepared for SEM by grinding using Stuers TegraPol-31 with Akasel Aka-piatto diamond grinding discs of incrementally higher grit until a mirror finish was achieved. Only the cross-section face, where the green sample had been broken, was studied. The coarser steps were important to make an even, flat surface and remove surface carbon from sintering. The samples were cleaned in an ultrasonic bath for 5 min and with ethanol between each step. The lubricant used was water and the samples were held by hand. The polishing steps were as follows:

1. MD-Piano 80, 6 min, 150 rpm
2. MD-Piano 220, 6 min, 150 rpm
3. MD-Piano 600, 6 min, 150 rpm

4. MD-Piano 1200, 3 min, 150 rpm
5. MD-Piano 2400, 3 min, 150 rpm

Image analysis of the polished surfaces was done using the ImageJ software (version 1.51s). The area fraction of pores was measured by thresholding. The greyscale histograms of the images and thresholds used are available in Appendix G Figure 9-1. The despeckle function was used to remove noise.

In addition, the fracture surfaces of the sintered samples were studied. The samples were broken using a hammer and once a suitable piece for SEM was obtained it was cleaned in ethanol in an ultrasonic bath for 10 min and mounted on an aluminium pin with carbon tape. For imaging, the Zeiss Supra 55 VP FE-SEM was used. The working distance was 10 mm and the high tension was 10 kV.

Phase analysis

The sintered samples were too large for the XRD sample holders available, so the samples were crushed to a powder using a hammer. The powder was sieved with a 500 μm mesh before characterisation.

The phase composition was analysed by X-ray diffraction. The samples were scanned in a D8 Advance DaVinci working in Bragg-Bernato geometry (2θ - θ). The diffractometer scanned from $2\theta = 20 – 80°$ for 30 minutes using V6. Copper K_α X-rays with wavelength 1.5406 nm were used. Obtained patterns were analysed using the Bruker EVA software and compared against patterns found in the International Centre for Diffraction Data (ICDD) in order to obtain phase composition. Both the powder materials and the sintered samples were analysed. Quantitative analysis was done using the Topas software (version 5) with Rietveld refinement.

4 Results

4.1 SiC slurries for solid-state sintering with Novolac

In this section, the results concerning the viscosity of SiC-Novolac slurries are presented. For ease of comparison, most figures present the dynamic viscosity at a shear rate of 40 s^{-1} if nothing else is specified. The data is also provided in Appendix B Table 9-2.

4.1.1 Effect of Hypermer KD7 concentration on the viscosity of SiC-Novolac slurries

The viscosity of SiC-Novolac slurries prepared with increasing amounts of Hypermer KD7 is presented in Figure 4-1.

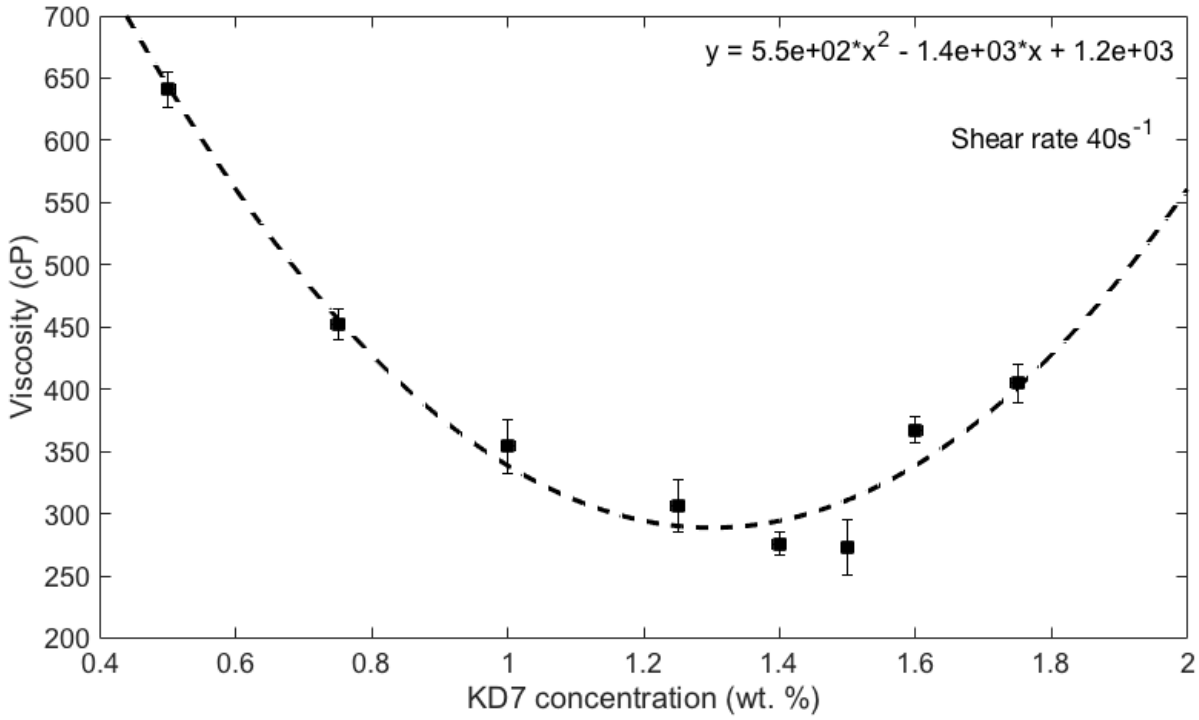

Figure 4-1 Viscosity of SiC-Novolac slurries at shear rate 40 s^{-1} as a function of Hypermer KD7 concentration. The solid loading was 72 wt. %, the binder content 5 wt. % and the pH ~9. The norm of residuals of the quadratic basic fitting was 55.7.

The viscosity decreased until it reached a minimum for a KD7 concentration of 1.5 wt. %. The minimum viscosity measured was 273 cP. Above 1.5 wt. % the viscosity increased again.

The quadratic fit had a norm of residuals of 55.7 and the calculated minimum was reached for 1.27 wt. %, somewhat lower than the experimental minimum.

In Figure 4-2 the viscosity and shear stress of the sample with the lowest viscosity is presented as a function of shear rate. The viscosity decreased exponentially with the shear rate as expected with shear thinning behaviour. The shear stress followed the Herschel-Bulkley model when increasing shear rate but there was slight thixotropy, so the shear stress was lower when decreasing the shear rate. The stress also fell slightly during the dwell time at 100 s^{-1}. The yield stress was 0.38 Pa, the consistency index was 1.7 and the flow index was 0.43. Because n < 1 the behaviour is considered pseudo-plastic. The yield stress was almost negligible in this sample.

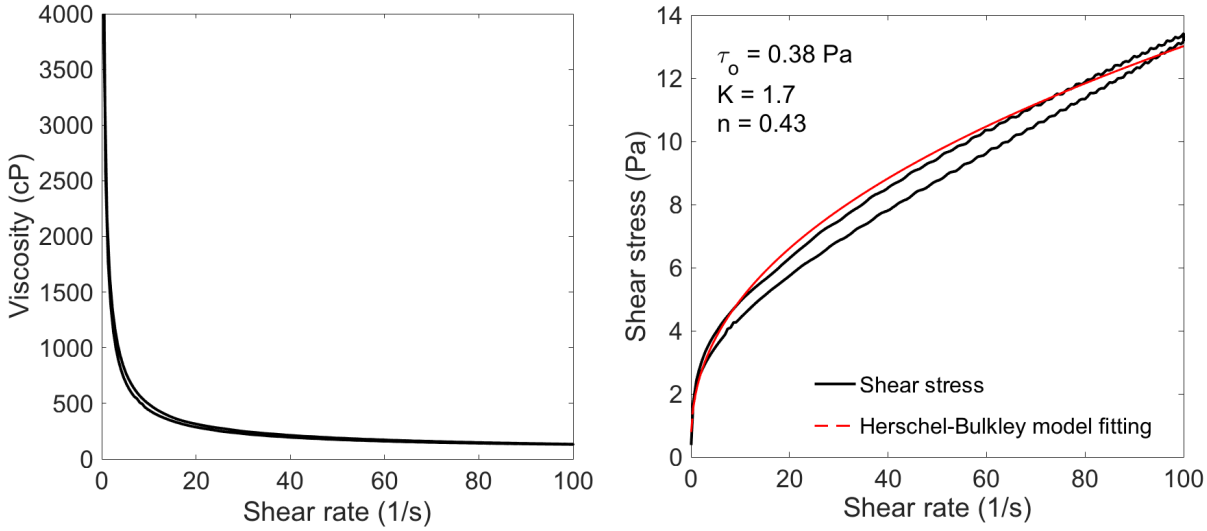

Figure 4-2 Viscosity and shear stress as a function of shear rate with Herschel-Bulkley model fitting for slurry sample SiCNovo72_1.50. The fitting parameters of the model are given.

4.1.2 Effect of solid concentration on the viscosity of SiC-Novolac slurries

The viscosity of SiC-Novolac slurries as a function of the solid loading is presented in Figure 4-3. The viscosity increased linearly with the percentage of solid loading and at 74 wt. % the viscosity was 402 cP. This is close to the practical limit for slip casting and the solid loading should then not be increased beyond 74 wt. %. The norm of residuals for the basic fitting was 8.6.

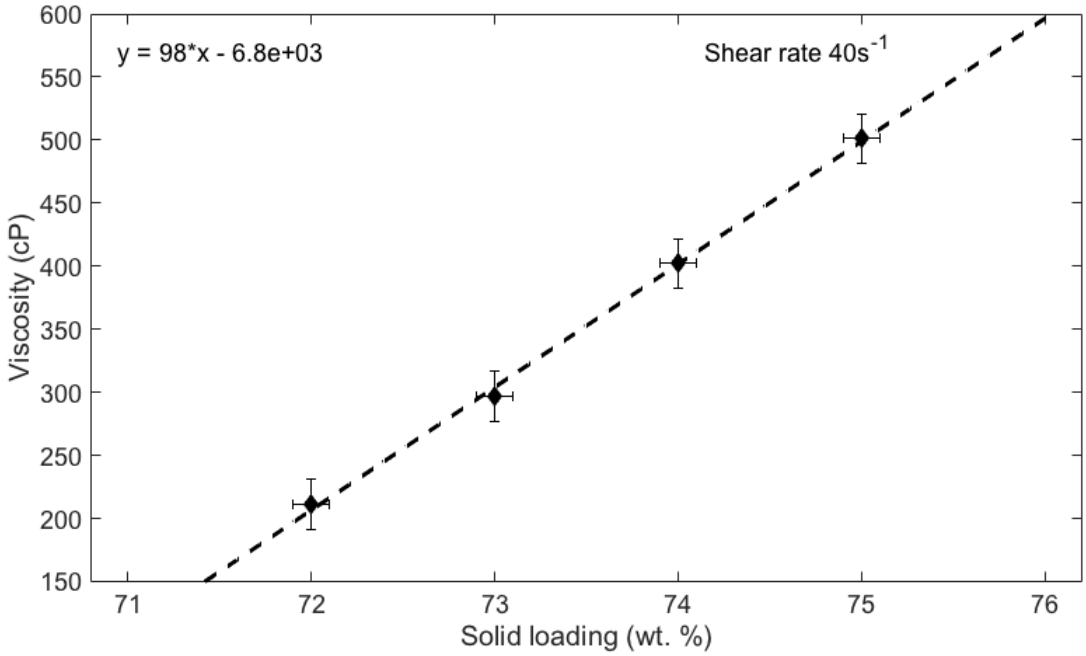

Figure 4-3 Viscosity of SiC-Novolac slurries increase with solid loading. The dispersant concentration was 1.5 wt. %, the binder content 5 wt. % and the pH ~9. Basic linear fitting had norm of residuals 8.6.

4.1.3 Effect of pH on the viscosity of SiC-Novolac slurries

The viscosity of SiC-Novolac slurries as a function of pH is presented in Figure 4-4. The viscosity reached a maximum for pH 9-9.5 and was lower for a pH closer to 8, at 176 cP. The viscosity decreased slightly when adjusting the pH to 10.

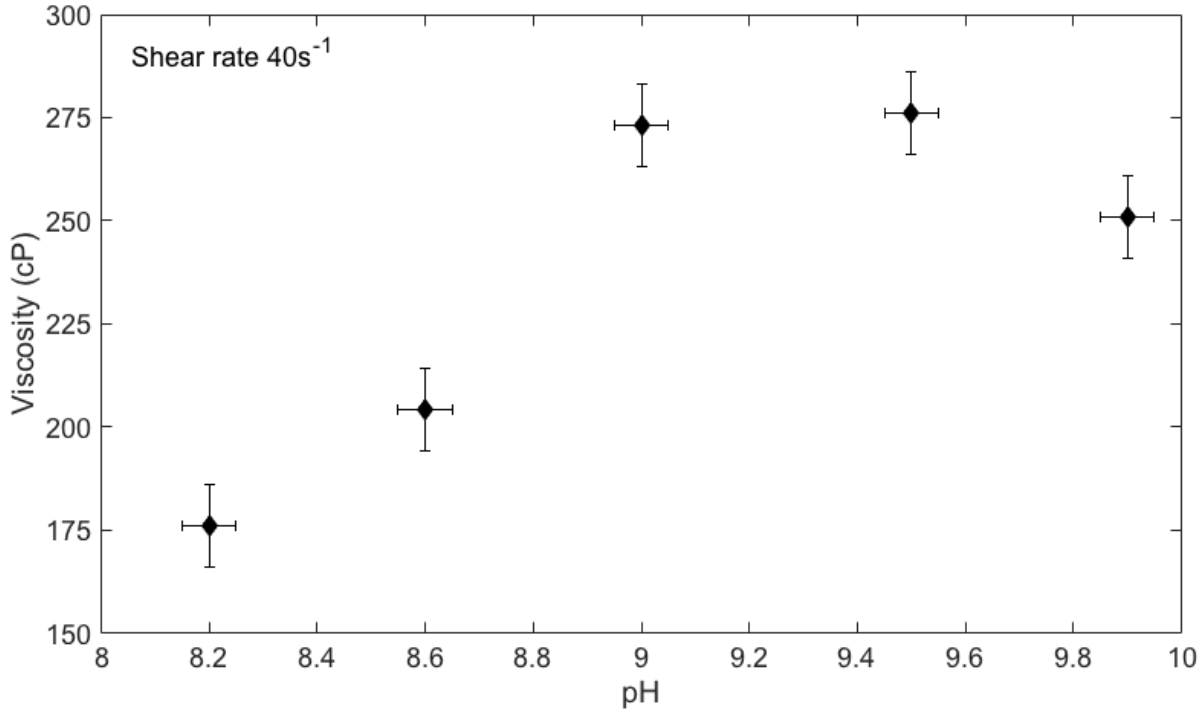

Figure 4-4 Change in viscosity of SiC-Novolac slurries with pH shows the viscosity is lower for pH values closer to 8. The solid loading was 72 wt. %, the dispersant concentration 1.5 wt. % and the binder content 5 wt. %.

4.1.4 Thermal decomposition of Novolac

The mass loss as a function of temperature in both air and argon atmospheres is presented in Figure 4-5. The mass loss was slow up to around 360 °C at which point the rate increased in both atmospheres. In air, the mass loss increased again for temperatures above 500 °C until all the material was burned away at 625 °C. In argon, the loss rate gradually slowed until the mass reached 47 % of the initial mass at 1000 °C. During the dwell time at this temperature, the mass continued to decrease until reaching 40 % of the initial mass.

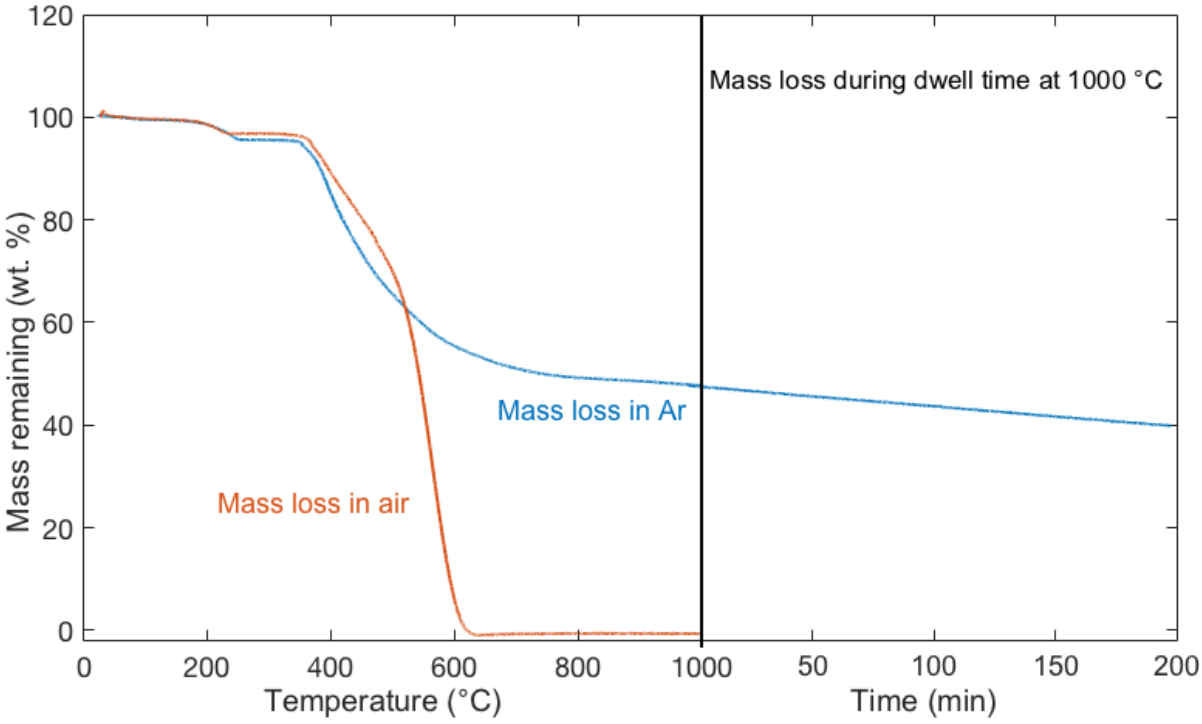

Figure 4-5 Thermal decomposition and pyrolysis of Novolac in air and argon illustrated by the mass lost as a function of temperature

4.2 SiC slurries for solid-state sintering with carbon black

In this section, the results pertaining to the viscosity of SiC-CB slurries are presented. As with the SiC-Novolac system, the dynamic viscosities are given for a shear rate of 40 s^{-1}. The results are also listed in Appendix B Table 9-2.

4.2.1 Effect of Hypermer KD7 concentration the viscosity of SiC-CB slurries

The viscosity of SiC-CB slurries at a shear rate of 40 s^{-1} as a function is given in Figure 4-6. The solid loading was 72 wt. % and the binder content was 5 wt. %. The pH was adjusted to 9 in all cases.

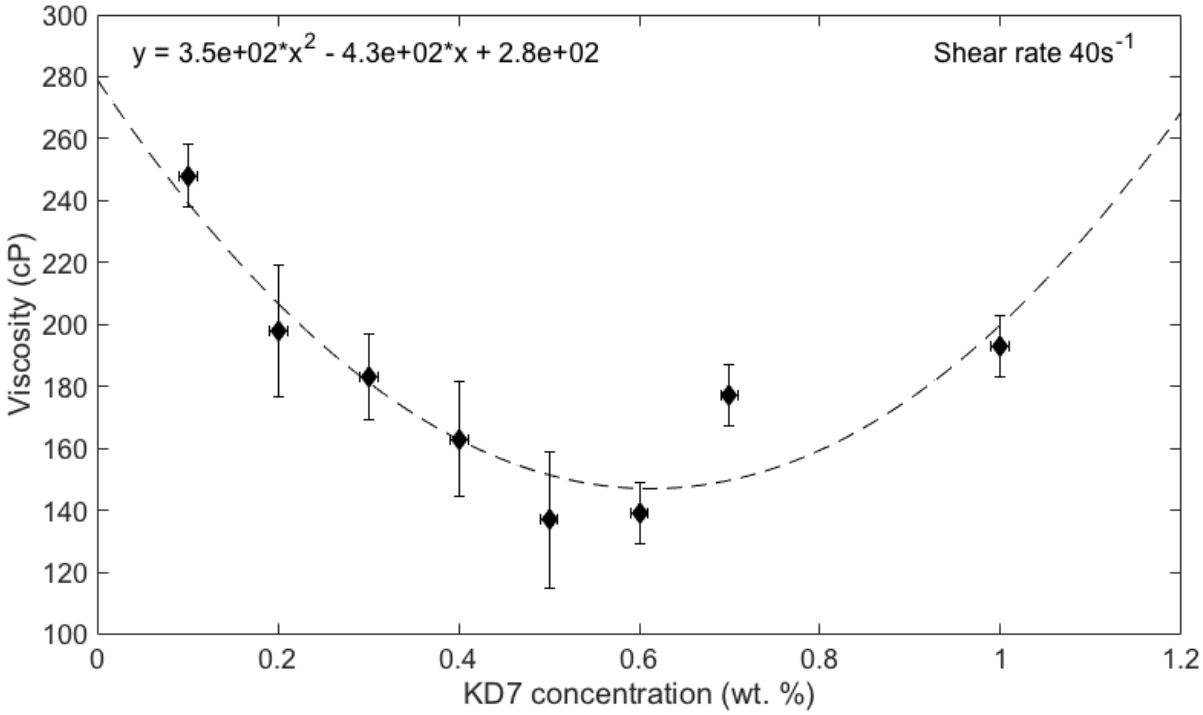

Figure 4-6 Viscosity of SiC-CB change as a function of Hypermer KD7 concentration at a shear rate of 40 s^{-1}. The solid loading was 72 wt. %, the binder content 5 wt. % and the pH ~9. The norm of residuals of the quadratic basic fitting was 34.9.

The dispersant was varied from 0.1 to 1 wt. % and the viscosity decreased until the concentration reached 0.5 wt. % at 137 cP. The viscosity increased for concentrations above this and evened out. All the measured values for viscosity were below 250 cP, a value considered reasonable for slip casting. The norm of residuals of the quadratic fitting was 34.9 and the minimum was for a concentration of 0.61 wt. % higher than the experimentally measured minimum.

4.2.2 Effect of solid loading on the viscosity of SiC-CB slurries

The viscosity of SiC-CB slurries as a function of the solid loading is presented in Figure 4-7. As expected the viscosity increased with increasing solid loading. The increase was close to linear up to 76 wt. % at which point the viscosity increased sharply from 340 cP to 654 cP for a solid loading of 77 wt. %. The increase then continued to increase at a similar rate. The viscosity remained below 400 cP for solid loading up to 76 wt. % which makes this the current limit for slip casting with this powder composition. The linear fitting for the viscosity from 72 to 76 wt. % had a norm of residuals of 30.8.

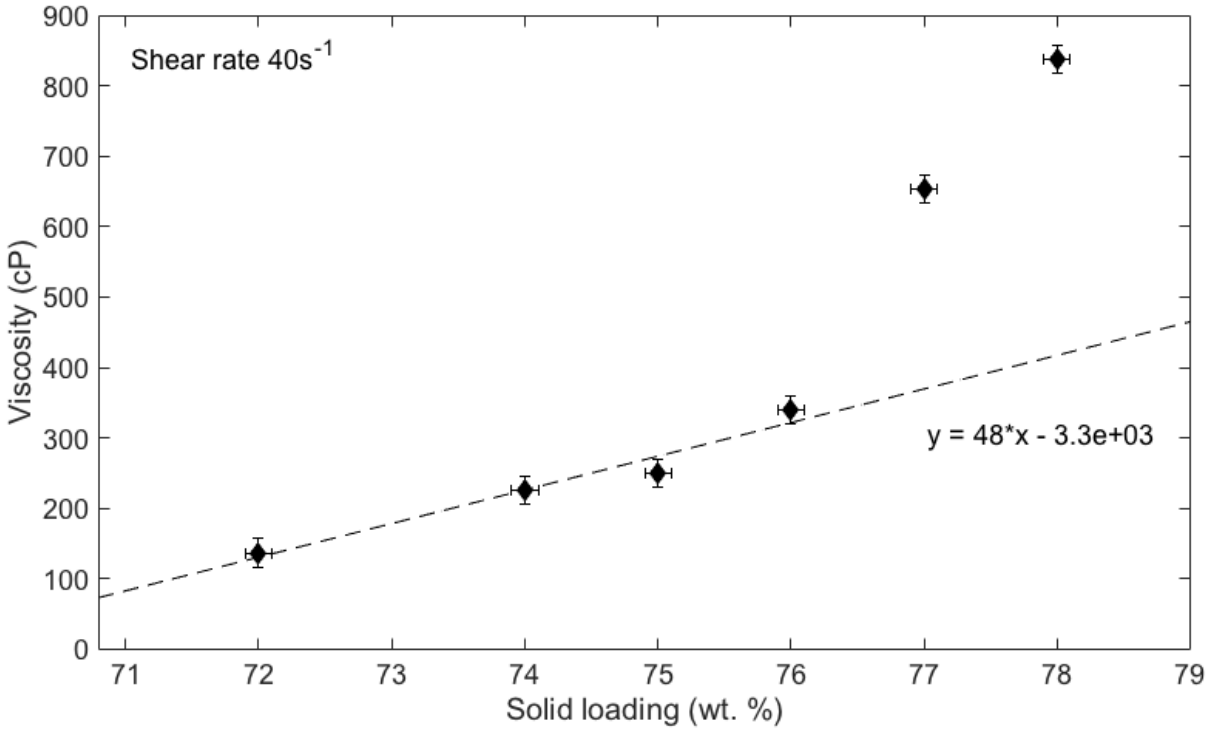

Figure 4-7 Increase in viscosity at shear rate 40 s^{-1} with solid loading in SiC-CB slurries. The dispersant concentration was 0.5 wt. %, the binder content 5 wt. % and the pH ~9. The shear rate was 40 s^{-1}. The linear basic fitting for the first 4 points had norm of residuals 30.8.

4.2.3 Effect of pH on the viscosity of SiC-CB slurries

In Figure 4-8 the viscosity of SiC-CB slurries as a function of pH is presented. The solid loading was 72 wt. %, the dispersant concentration was 0.5 wt. % and the binder content was 5 wt. %. The viscosity decreased from pH 8 to 9 and remained low for higher pH values so keeping the pH close to 9 is necessary to minimize viscosity.

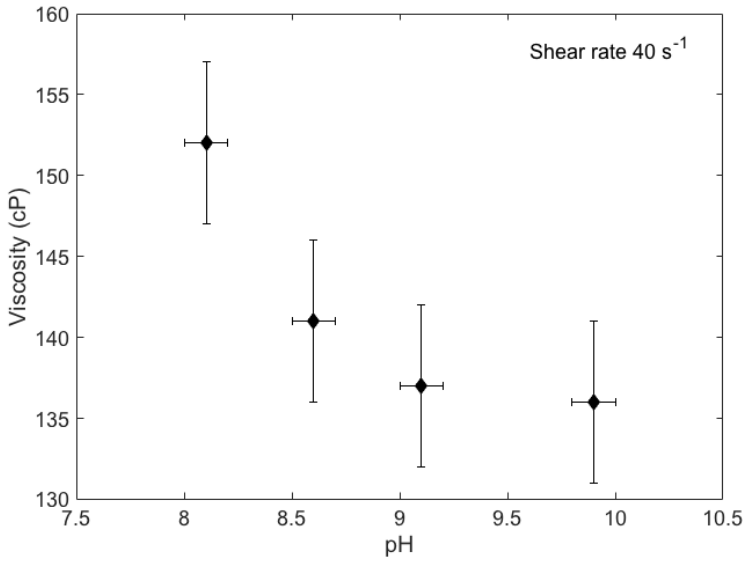

Figure 4-8 Decrease in dynamic viscosity at shear rate 40 s^{-1} with increasing pH for SiC-CB slurries with solid loading 72 wt. %, 0.5 wt. % Hypermer KD7 and 5 wt. % binder.

4.3 Characteristics of slip cast SiC green bodies

4.3.1 Appearance and general comments

Figure 4-9 shows a selection of the green bodies made during the course of the study. For lower solid loading there were few defects, though large pores could be observed on the surface most likely due failure to remove air in the slurry prior to casting. There was a white powder residue on the surface that can be attributed to the BN-talc mixture used on the mould to prevent sticking. In addition, the SiC-Novolac samples were much lighter in colour than the SiC-CB due to the yellow colour of Novolac compared to the colour of carbon black.

Increasing the solid loading to 74 and 76 wt. % for SiC-Novolac and SiC-CB respectively led to an increase in surface defects presented as cavitation and some cracking in those areas as seen in Figure 4-9 (a). All the green bodies had high strength, especially after drying, so they could easily be handled without breaking. In fact, to successfully break the bars into smaller pieces, it was necessary to use a hacksaw to saw part of the way through the bar before fracture would occur. The weakest points were the edges that could chip, often while demoulding.

The first couple of casting attempts were unsuccessful because the volume of the slurry was too low and resulted in a “tunnel” in the top half of the bar. This was due to the capillary

forces adsorbing the water in the slurry and inducing a controlled settling of the particles along the sides of the mould. Increasing the amount from 250 to 400 g of powder to make a larger volume of slip corrected this issue.

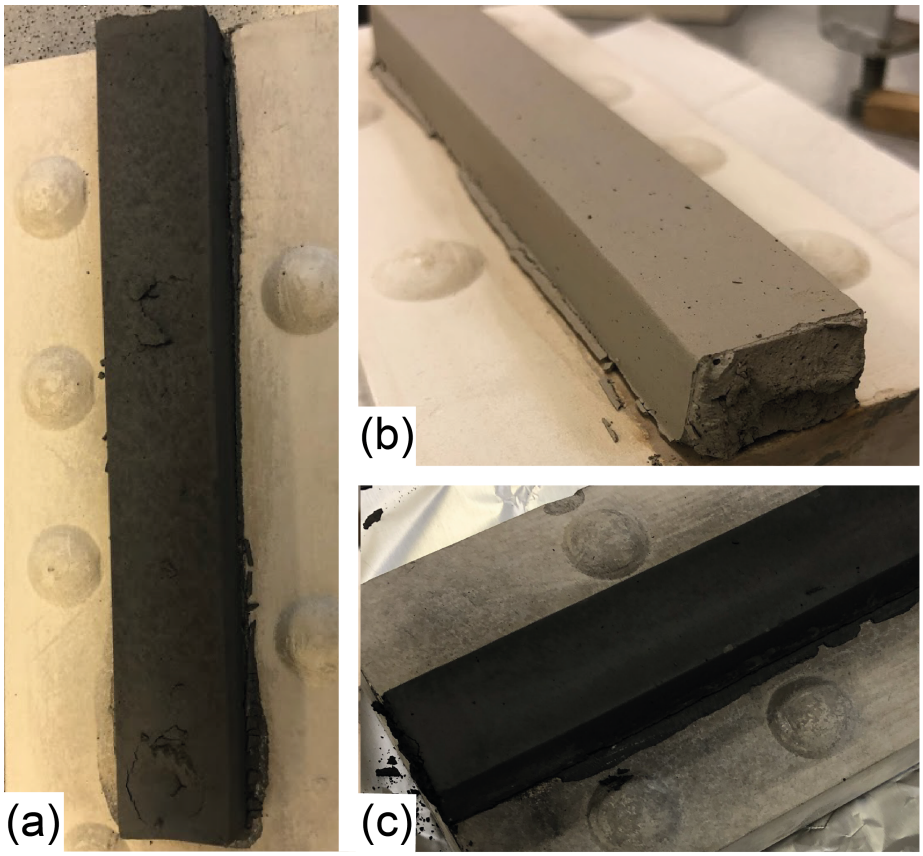

Figure 4-9 Examples of slip cast green bodies after demoulding. (a) is an example of cavitation and surface defects in a SiC-CB green body with 76 wt. % solid loading. (b) and (c) show more typical green bodies for SiC-Novolac and SiC-CB respectively. SiC-Novolac had a lighter colour due to the yellow of the Novolac powder.

4.3.2 Thermal behaviour

The thermogravimetric measurement of SiC-CB and SiC-Novolac green body samples is given in Figure 4-10. For SiC-CB a 2.5 wt. % mass loss was measured between 300 and 400 °C. From 400 to 1200 °C the weight remained constant before decreasing again above this temperature. The mass decreased by 1.5 wt. % between 1200 and 1400 °C and the dwell time led to a further decrease of 1 wt. % reaching a final weight of 94 wt. % of the starting weight.

For SiC-Novolac the mass lost was much higher and the weight increased between 700 and 1200 °C and again during the dwell time. There was a mass loss over 6 % during heating to

700 °C, and when the temperature reached 1400 °C 92 % of the initial mass remained. The mass decreased further up to 1 hour into the dwell time, then increased slightly over the course of 3 hours.

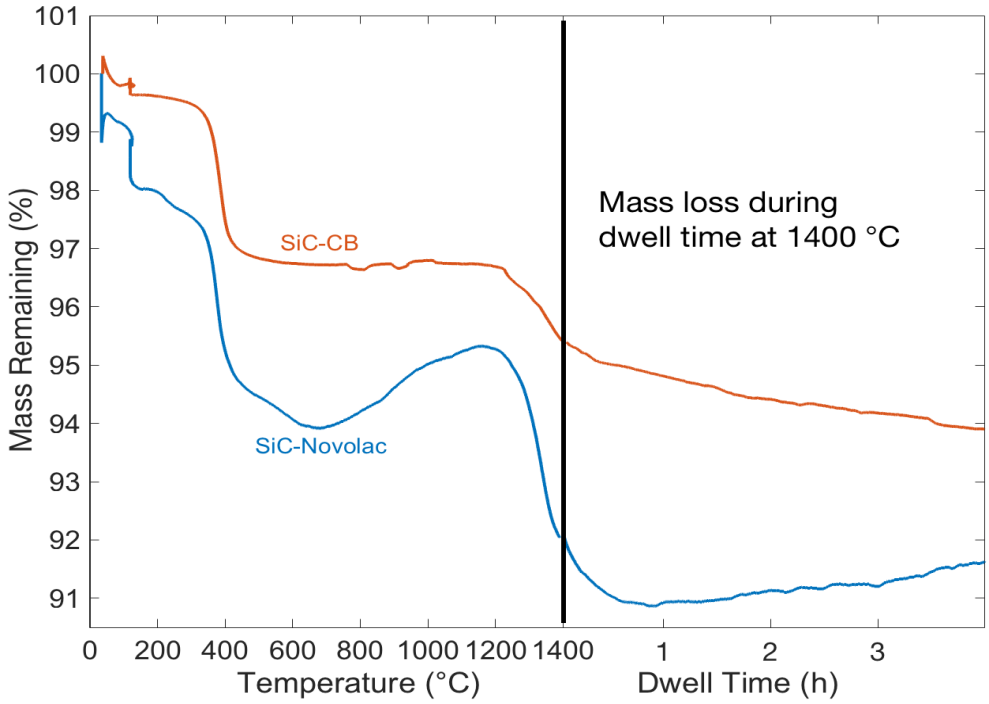

Figure 4-10 SiC-Novolac and SiC-CB green body mass loss during heating to 1400 °C in Ar. The binder burnout occurs at 400 °C and the pyrolysis of Novolac between 400 and 800 °C. SiO_2 decomposition starts at 1300 °C. The mass loss is higher for SiC-Novolac because of pyrolysis of the polymer carbon additive.

4.3.3 Green body density

The green body densities of SiC-CB and SiC-Novolac samples (marked with orange squares and blue diamonds respectively) with different solid loadings are presented in Figure 4-11. The highest relative density of 55.8 % was achieved for the SiC-CB green bodies with a 75 wt. % solid loading. The average relative density was 54.4 % for a 75 wt. % solid loading, and 51.5 % for a 76 wt. % solid loading. Thus, increasing the solid loading to 76 wt. % did not increase the green body density.

The SiC-Novolac green bodies had an average relative density of 48.9 % for a solid loading of 72 wt. %. For a solid loading of 74 wt. % the average density was 46.5 % but a couple of samples reached relative densities as high as 50 %. As with SiC-CB, increasing the solid loading did not increase the green body density on average.

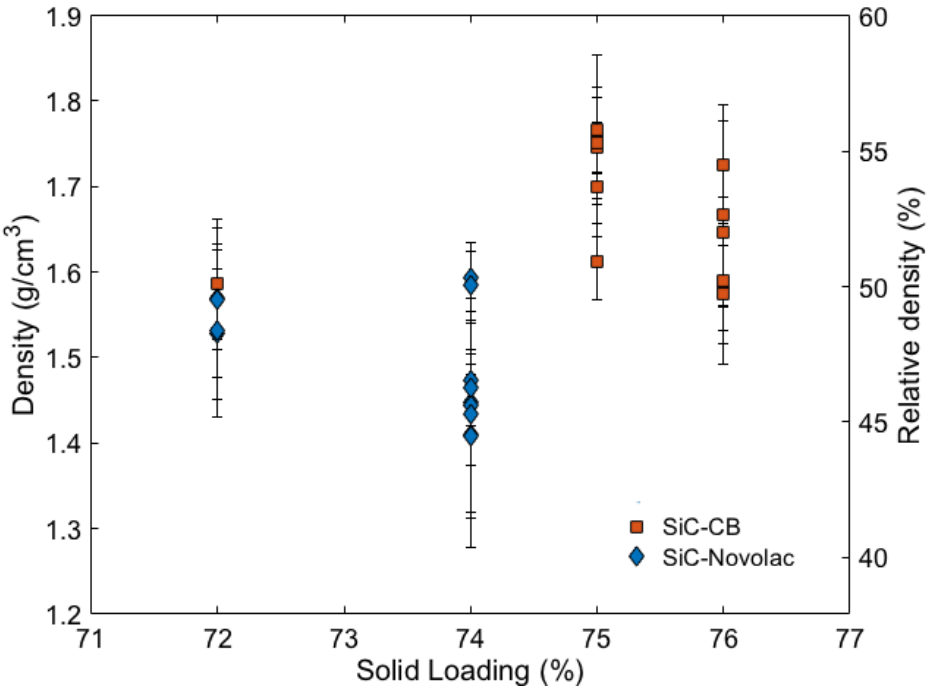

Figure 4-11 Green density of SiC-CB and SiC-Novolac slip cast green samples for different solid loadings. SiC-CB is marked with orange squares and SiC-Novolac with blue diamonds. The error bars represent the standard deviation in the calculated geometric density.

The variation in green body density for the different samples is given in Figure 4-12. There are slight differences in density throughout the samples for all the samples. The smallest variation occurs in a SiC-CB sample with 76 wt. % solid loading. The trend in most samples was a 2 % decrease in density from bottom to the top. In one SiC-Novolac sample with 74 wt. % solid loading the density in the top was 4 % lower than at the bottom of the sample. The density gradients were not consistently reduced by increased solid loading.

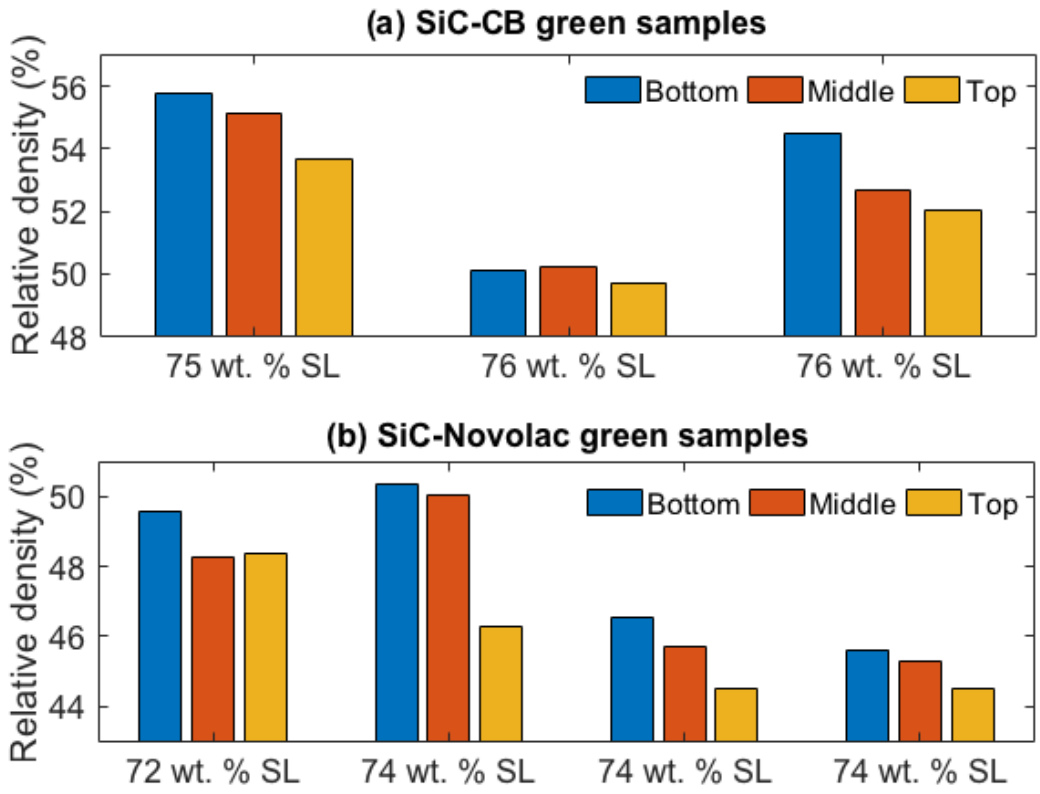

Figure 4-12 Green density in different positions in the samples. SiC-CB and SiC-Novolac are shown in (a) and (b) respectively and the solid loading (SL) of the sample is specified below.

4.3.4 Fracture surface morphology

In Figure 4-13 and Figure 4-14 the SEM images of SiC-CB and SiC-Novolac green bodies, respectively, are presented. Image (b) in both figures reveal that both samples have SiC grains, on average, 1 µm in size with a wide distribution in size from 200 nm to 2 µm. The particles were highly faceted and slightly anisotropic. Some large pores were present ranging from 2 to 20 µm in diameter and a few were smaller than 1 µm. Image (c) in both figures have some particles 100 nm in size.

Image (a) in Figure 4-13 shows the fracture surface of the SiC-CB green sample has a few ridges and is very uneven while the SiC-Novolac green sample is much smoother as seen in Figure 4-14 (a). The particles are tightly packed in the binder matrix in both samples.

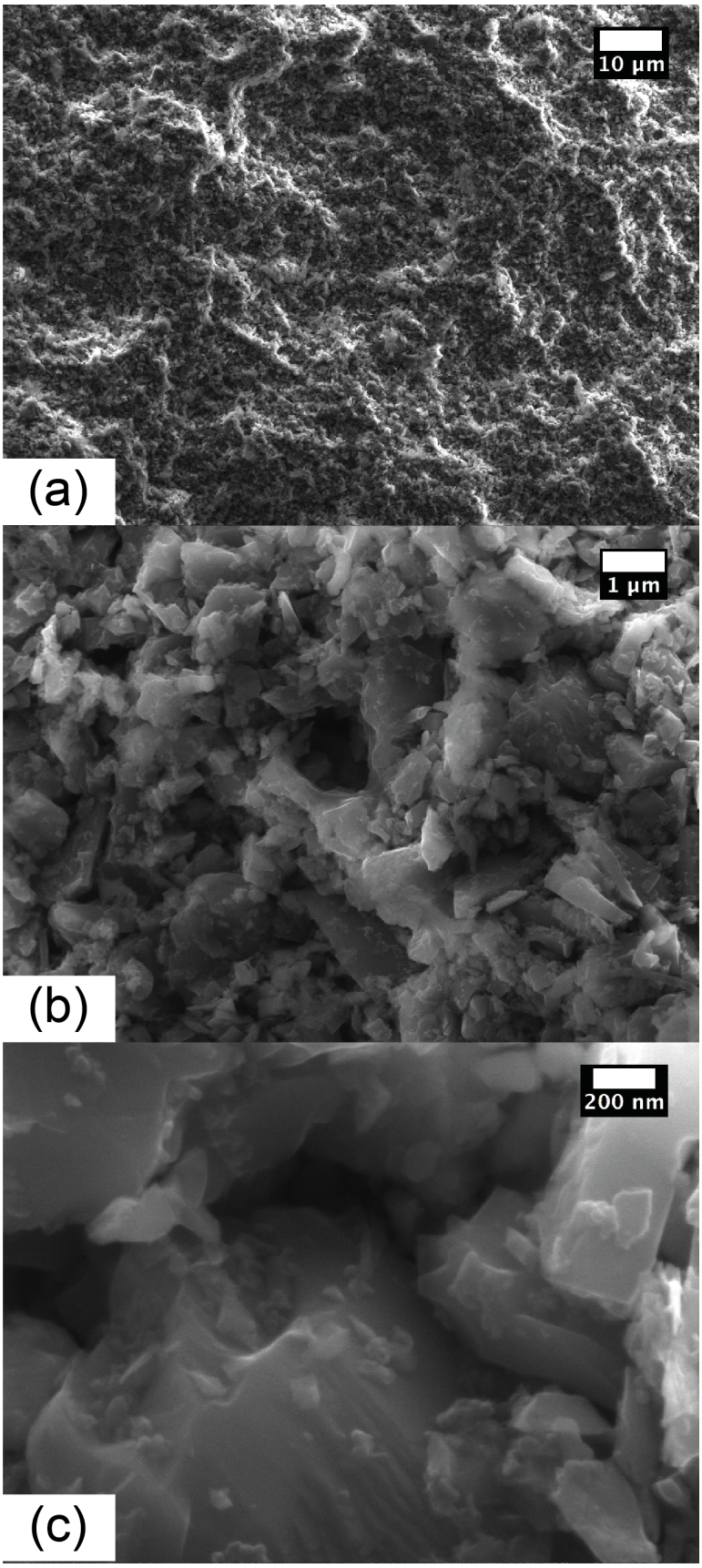

Figure 4-13 SEM images of a SiC-CB slip cast green body

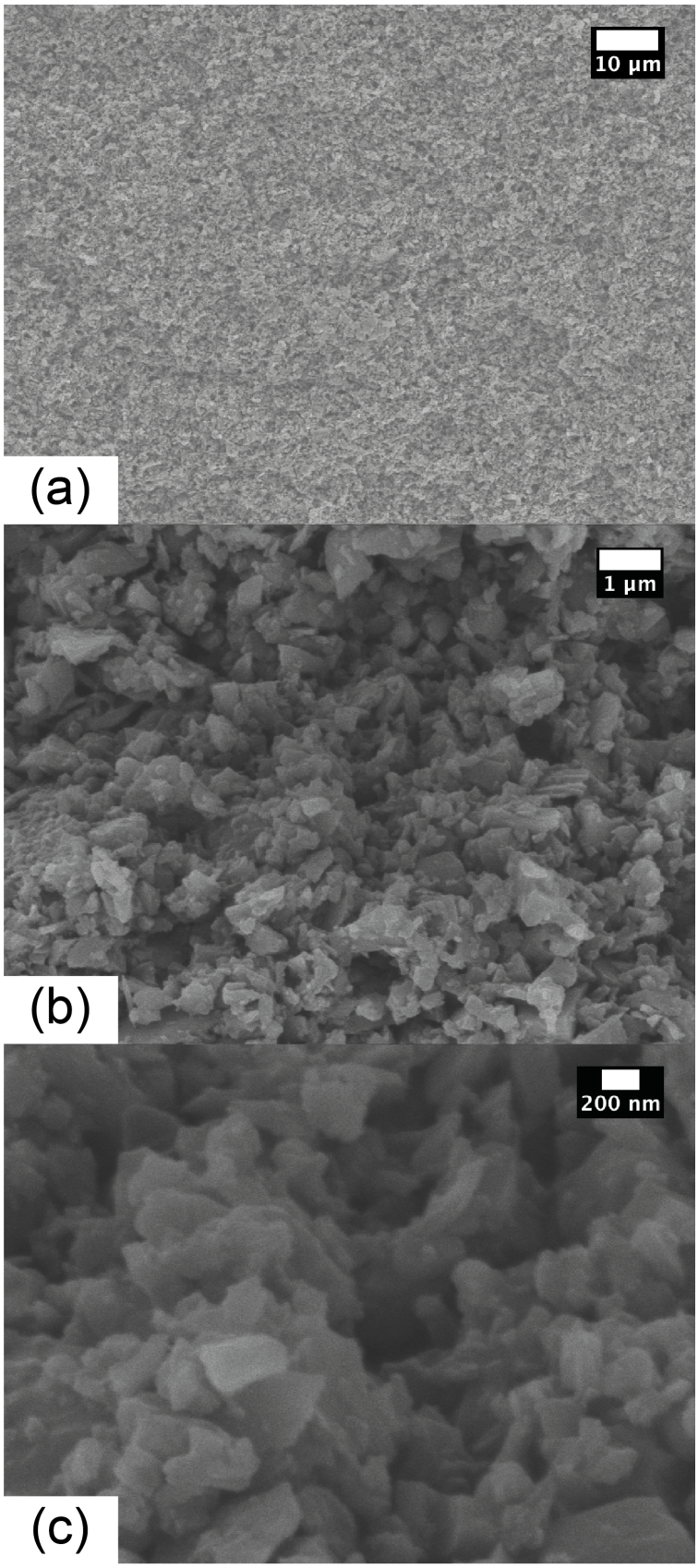

Figure 4-14 SEM images of a SiC-Novolac green body

4.4 Sintered body characterisation

4.4.1 Sintered density and linear shrinkage

The bulk densities of sintered SiC-CB and SiC-Novolac samples as a function solid loading are presented in Figure 4-15. The highest density of 97.8 % TD was achieved for SiC-CB with a solid loading of 75 wt. %. The lowest SiC-CB density was 93 % TD for a solid loading of 72 wt. %. The sintered density of SiC-Novolac was overall lower than for SiC-CB with the highest value being 93.5 % TD.

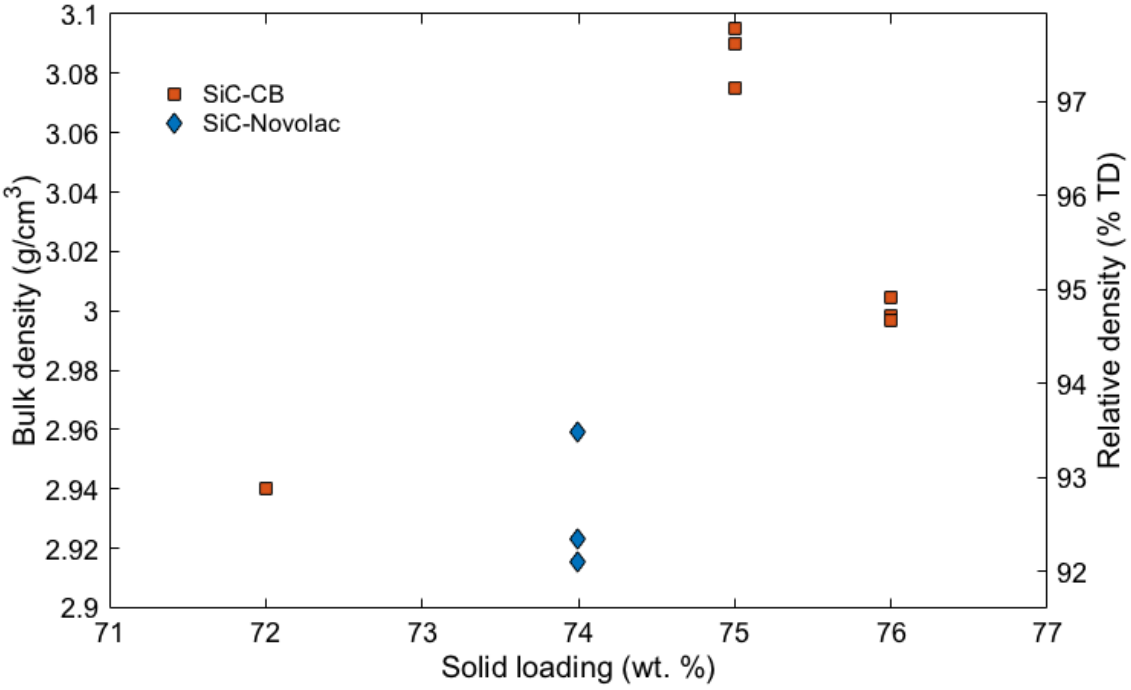

Figure 4-15 Sintered density of SiC-CB and SiC-Novolac samples as a funciton of solid loading. All data are provided in Appendix F.

The open and closed porosity of the different sintered samples is given in Figure 4-16. The total porosity was highest in the SiC-Novolac sample at close to 8 %, and 1-2.5 % open porosity. In the SiC-CB sample with 76 wt. % solid loading the porosity was constant throughout the sample at ~5 %. In the SiC-CB with 75 wt. % solid loading the porosity increased from bottom to the top from 2.2 % to 2.9 %. The fraction of total porosity that was open increased in the top section of the sample from 20 % to almost 50 %.

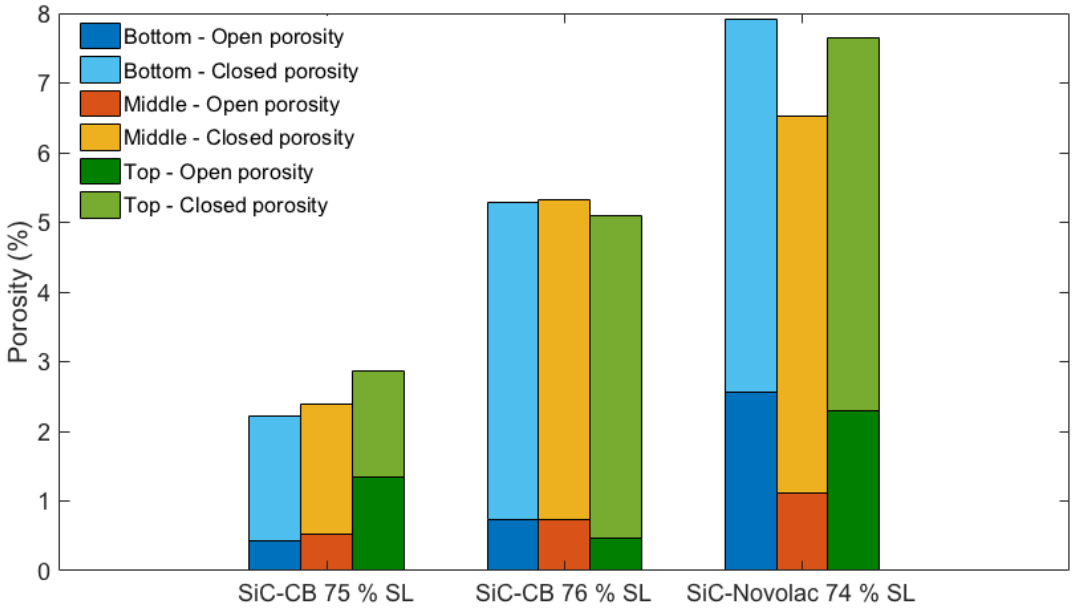

Figure 4-16 Open and closed porosity in the sintered samples of given solid loading and carbon additive. All data are provided in Appendix F.

The linear shrinkage of each sample as a function of the green body density is given in Figure 4-17. The linear fitting shows the shrinkage is reduced by increased green body density. The norm of residuals of the linear fitting was 4.42. The lowest linear shrinkage of 17.7 % was achieved for the samples with the highest green body density. The shrinkage was higher in the SiC-Novolac samples than the SiC-CB even for similar green body densities with the highest degree of shrinkage being 22.5 %.

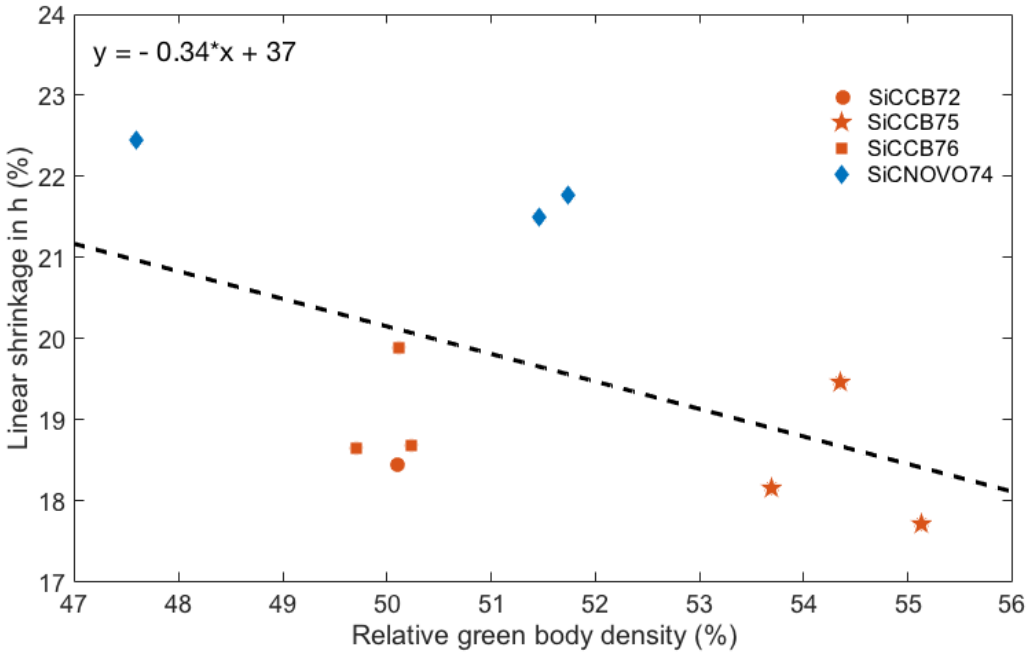

Figure 4-17 Decrease in linear shrinkage in h as a function of increase in green body density of sintered SiC-CB and SiC-Novolac with different solid loadings. Line corresponds to a linear basic fitting of all the points.

4.4.2 Polished and fracture surface characteristics

SEM images of polished SiC-CB and SiC-Novolac sample surfaced are presented in Figure 4-18. The darker spots are porosity. Image analysis by thresholding in ImageJ determined the porosity to be 6.5 % in SiC-CB and 5.1 % in SiC-Novolac. The true porosity of this SiC-CB sample measured by the Archimedes method was 4.21 %. The true porosity of the SiC-Novolac sample was 7.64 %.

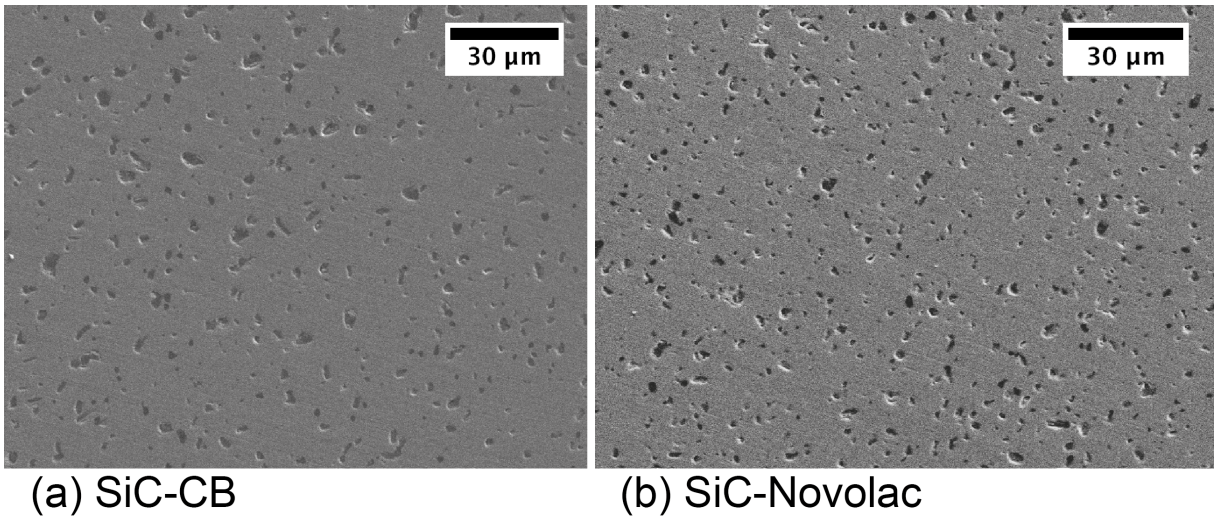

Figure 4-18 SEM micrographs of the polished surfaces of sintered SiC-CB (a) and SiC-Novolac (b). The dark spots are pores in the samples.

SEM micrographs of the fracture surface of sintered SiC-CB and SiC-Novolac are presented in Figure 4-19. There were a few differences between the two samples. Firstly, the SiC-CB sample had a much smoother surface than SiC-Novolac, characteristic of transgranular fracture. SiC-Novolac, on the other hand was much more faceted and textured. This indicates a higher degree of intergranular fracture. Both samples presented some evidence of tearing-open and pulling-out mechanisms.

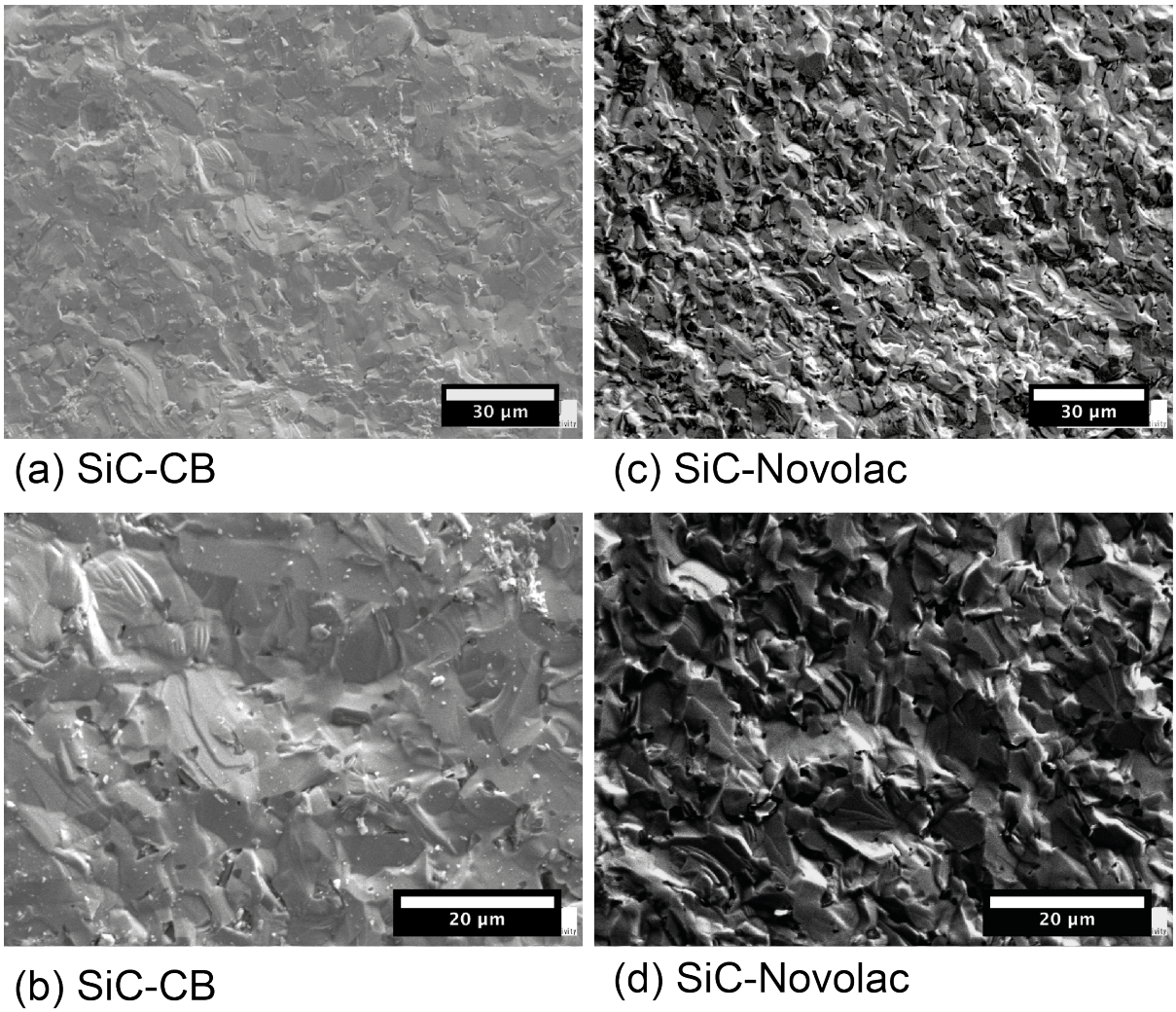

Figure 4-19 Fracture surfaces of sintered SiC-CB (a and b) and SiC-Novolac (c and d). The smoothness in (a) and (b) is indicative of transgranular fracture while (c) and (d) have more intergranular fracture. Some tearing open and pulling-out mechanisms can be observed in both samples.

4.4.3 Phase composition

The stacked XRD spectrum of SiC-CB is presented in Figure 4-20 with the raw powder at the bottom and the sintered sample on top. There a few peaks that appeared after sintering that correspond to different polytypes of SiC. In the raw powder, only the α-SiC phase (6H-SiC) was present while the sintered sample had other hexagonal polytypes (4H- and 2H-SiC).

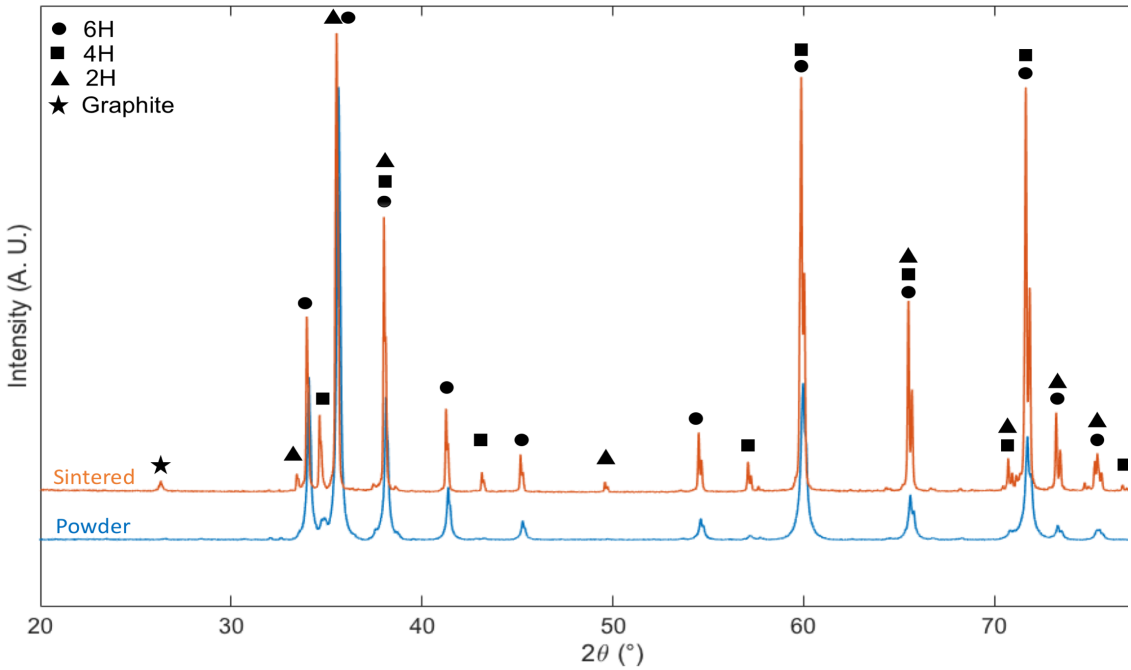

Figure 4-20 XRD-spectra of SiC-CB raw powder and sintered SiC-CB. 6H (PDF 04-010-5698) is marked by a circle, 4H (PDF 04-010-5697) by a square, 2H (PDF 00-029-1130) by a triangle and graphite (PDF 00-001-0640) by a star.

The peaks corresponding to the different polytypes are marked with different symbols in the figure: circle for 6H-SiC, square for 4H-SiC and triangle for 2H-SiC. In addition, some graphite was present in the sintered sample, marked by a star. The intensity of the peaks increased for the sintered sample compared to the raw powder, especially at higher angles.

The stacked XRD spectrum of SiC-Novolac is presented in Figure 4-21 with the raw material powder at the bottom and the sintered sample on top. As with the SiC-CB sample, there was 2H and 4H-SiC present in the sintered sample.

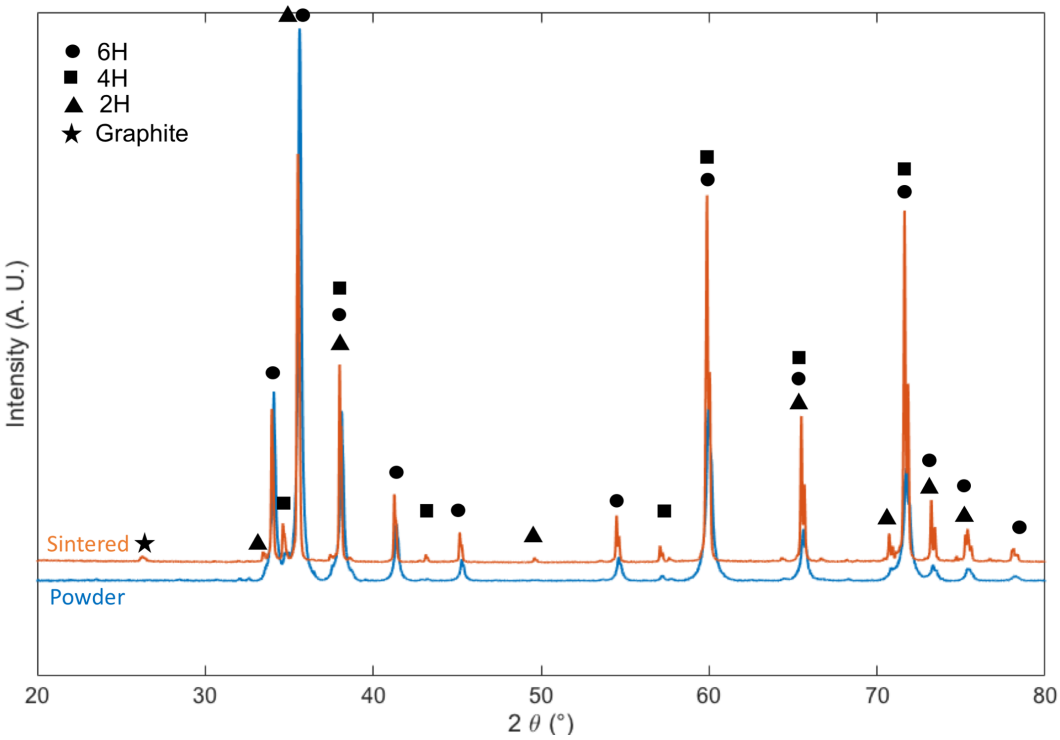

Figure 4-21 XRD spectra of SiC-Novolac raw powder and sintered SiC-Novolac. 6H (PDF 04-010-5698) is marked by a circle, 4H (PDF 04-010-5697) by a square, 2H (PDF 00-029-1130) by a triangle and graphite (PDF 00-001-0640) by a star.

The ratio between the different phases present was examined in Topas by Rietveld structure fitting assuming that only 6H and 4H were the only polytypes present. The amounts of phases are listed in Table 4-1. The amount of 4H was only slightly higher for the SiC-CB sample and 6H was the major polytype in both samples. The values may not exact and could vary up to 15 % with different parameters chosen for the structure fitting.

Table 4-1 The relative amount of the 6H and 4H polytypes in sintered samples measured by Rietveld fitting in Topas assuming these are the only polytypes present.

Material	**4H (wt. %)**	**6H (wt. %)**
Sintered SiC-CB	20	80
Sintered SiC-Novolac	14	86

5 Discussion

5.1 Thermal decomposition of Novolac

The thermal decomposition of Novolac is important to understand in order to know the amount of carbon expected to be present during sintering. The TGA result presented in Figure 4-5 revealed that in argon 47 wt. % of the mass remained after heating to 1000 °C. In both atmospheres, the mass decreased initially due to release of moisture, free phenol, and aldehydes up to 350 °C. Above this temperature, the polymer began to decompose and in air the heating led to complete fragmentation into volatile products and no material remained above 600 °C. If the Novolac contained any inorganic matter such as polymer fillers these would remain after heating to 1000 °C. According to these results, no such impurities are present and only the carbon would remain during sintering in argon.

The mass loss in argon slowed considerably for temperatures above 750 °C but the mass was still decreasing. This mass loss is also present during the dwell time at 1000 °C at the same rate. At the end of the dwell time, the remaining mass remaining was just 40 wt. %. This could be due to some slight oxidation due to impurities in the argon gas. If taken into consideration the expected carbon yield of Novolac could be lower than these results show since the temperature in the sintering programme goes as high as 2150 °C.

A study on the pyrolysis of phenolic resin in SiC granules argued that high gas flow rate can increase carbon yield. [68] The TGA experiments were performed with a constant flow rate of argon at 30 ml/min (1.8 L/h). However, the flow rate of argon during sintering was between 20 and 300 L/h, much higher than the TG measurements. It is therefore uncertain if the carbon yield measured is exact, which could lead to excess carbon in the sintered SiC-Novolac samples.

5.2 Optimization of SiC slurry viscosity

5.2.1 Effect of dispersant concentration

For both the SiC-CB and the SiC-Novolac systems the viscosity was measured as a function of Hypermer KD7 concentration. The results presented in Figure 4-1 and Figure 4-6 show the viscosities reach a minimum for a certain concentration of dispersant and in both cases the

viscosity increases for concentrations under and above this ideal value. This behaviour is consistent with most ceramic colloidal dispersions. The decrease in viscosity was accompanied by a comparable decrease in yield stress and thixotropy. The measured ideal concentration of dispersant was 0.5 wt. % for SiC-CB and 1.5 wt. % for SiC-Novolac.

The decrease in viscosity for lower concentrations of dispersant can be explained by the increase in surface coverage density of the polymeric dispersant. For lower concentrations, the number of polymer chains in solution was insufficient to properly stabilize the suspension leading to higher viscosity. In addition, the partial coverage of the particle surface could lead to bridging flocculation. This is especially pertinent in cases where the polymer has a slight affinity to the particle.

At the ideal concentration, the polymer chains could supply sufficient repulsive forces to keep the particles from agglomerating and thereby minimizing the viscosity. At high dispersant concentration, several mechanisms could lead to increased viscosity. One possibility is depletion flocculation where there is a large concentration of the polymer in the bulk and a low concentration between the particles creating an osmotic pressure difference. The pressure leads liquid to flow out of the gap between particles allowing them to agglomerate. Another effect could be the high polymer concentration leading to entanglement of the long polymer chains in a similar fashion to gel-formation.

The difference in the required concentration of dispersant to minimize viscosity in SiC-CB and SiC-Novolac can be attributed to the specific surface area of the powders. The surface area of both the Novolac and carbon black powders can be considered a large contribution to the total specific surface area of the powder mixes and the concentration of Novolac in the mix is higher than the concentration of carbon black (7 wt. % compared to 3 wt.% for carbon black). Thus, if the dispersant concentration were to be normalized to mass per surface area of coverage the required concentration for minimum viscosity would probably be more similar for SiC-CB and SiC-Novolac.

5.2.2 Increasing the solid loading of SiC slurries

Figure 4-3 and Figure 4-7 the viscosities as a function of solid loading were presented. The viscosity of the SiC-Novolac slurries was significantly higher than for SiC-CB. At a 74 wt. % solid load the viscosity was 226 cP for SiC-CB and 402 cP for SiC-Novolac. For viscosities

above 400 cP at shear rate 40 s^{-1} the slips become difficult to cast. Thus, the maximum solid loading possible was 74 wt. % for SiC-Novolac slurries and 76 wt. % for SiC-CB slurries. These values are an increase of 2 wt. % and 1 wt. % compared with the solid loading that had been achieved when this study started.

The viscosity of SiC-Novolac slurries increased linearly with solid loading. In the SiC-CB slurries, the viscosity increased linearly from 72 to 76 wt. % solid loading. The significant increase in viscosity at 77 wt. % is due to the increase of interparticle effects and the friction between particles leading to decreased flow.

Fitting of the data points can be done with the Krieger-Dougherty (KD) model given in equation (2.19) as shown in Figure 5-1. The coefficient B (2.5 for spheres) is expected to increase as the anisotropy of the solid phase increases. With values for B at 5.8 and 6.4 for SiC-CB and SiC-Novolac respectively, the solid phase can be considered highly anisotropic, which is expected with SiC particles. The parameter $\phi_m = 0.62$, is slightly lower than the for random close packing of spheres (0.64). The viscosity of SiC-Novolac was still higher than SiC-CB even when adjusting for powder density and plotting by volume fraction. This could be due to the higher relative number of small particles. Both carbon black and Novolac have primary particle sizes in the nanometre scale (30-100 nm). There is, however, a higher concentration of these in the SiC-Novolac slurries. These can contribute to the increased shear stress by packing between larger particles and reducing the freedom of movement of the particles.

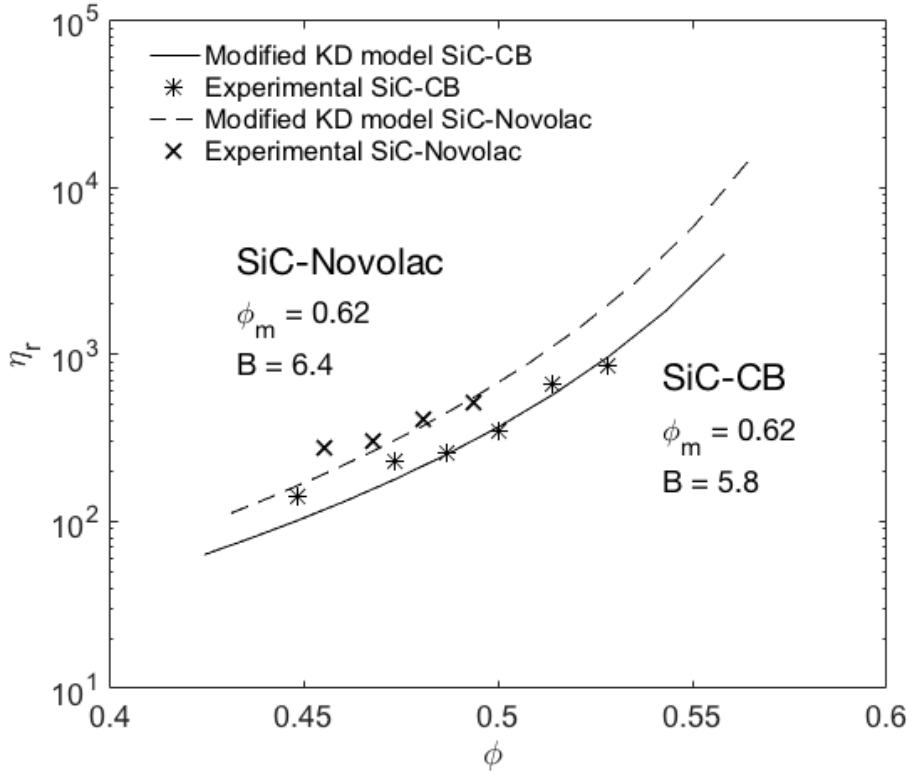

Figure 5-1 Relative viscosity of SiC-CB and SiC-Novolac slurries measured at 40 s^{-1} as a function of the volume fraction. Modified KD model with given fitting parameters.

The accuracy on the model fitting can be discussed as it does not take into account the presence of polymers in the fluid and assumes only water as the continuous phase. The dispersant and the binder in the slurry will have an impact on the relative viscosity and we could expect a lower value for B in both slurries.

5.2.3 The influence of pH on slurry rheology

As mentioned previously, the pH of most of the slurries was adjusted to 9 in order to ensure the stabilizing effect of the negative surface charge. The results presented in Figure 4-4 show that the SiC-Novolac slurries are highly sensitive to pH as it affects the solubility of the Novolac in water. This effect had not been considered before most of the measurements had been done. However, the results clearly show a decrease in viscosity when keeping the pH closer to 8.

The dissolution of Novolac mentioned in Section 2.3.2 is the most likely explanation for this effect. The phenolic hydroxyl groups are susceptible to deprotonation that leads to a partial dissolution of the particle in high pH aqueous solutions. The dissolution is characterised by a

swelling of the particle and reduced glass transition temperature. [69] This particle modification can manifest as “stickiness” of the slurry and tendency to form large agglomerates, possibly accounting for the higher viscosity of the SiC-Novolac slurries, compared to SiC-CB. In addition, the formation of phenolic strings in the presence of hydrogen acceptors has been shown to increase viscosity. [70] These strings can act as long polymer chains through the slurry, impeding the free movement of particles and thereby decrease viscosity.

The partial dissolution of Novolac in water could also decrease the final amount of carbon in the green body as the water is drawn out by capillary forces. There is, however, no indication that this effect is significant enough to warrant increasing the amount of Novolac in the powder mixture.

The viscosity of SiC-CB slurries decreased with increasing pH as shown in Figure 4-8. This behaviour is common in SiC slurries and due to the increased electrostatic repulsion provided by the EDL. Higher pH can favour the deprotonation of surface oxide groups and increases the absolute value of the zeta potential.

5.3 Slip cast green bodies characteristics

5.3.1 Appearance and general characteristics

The quality of slip cast green bodies is determined by several parameters. Firstly, the visual inspection of the surface and cross-section can be an initial insight into flaws present in the product. The green bodies presented in Figure 4-9 (b) and (c) were examples of successful casts are there were no cracks or important surface flaws. The most important issue was the presence of large pores that are attributed to air trapped in the slurry. Removal of trapped air is an engineering problem that can be solved by special equipment, such as a vacuum mixer.

The cavitation and surface cracks present in the green bodies with higher solid loading, seen in Figure 4-9 (a), could be due to a combination of the higher viscosity of the slurries and the high packing of solid reducing the freedom of movement of the particles. The silicone reservoir used was supposed to ensure the mould was continuously filled as water was drawn out. However, the increased solid loading and increased viscosity of the slurries could impede this, thereby essentially clogging the path for material to flow throughout. As water was

drawn out this resulted in hollow spots in the bottom of the body and finally cavitation and cracking in this area.

The high strength of the green bodies was noted, though not measured. This is mostly due to the high concentration of binder used, and an indication that the binder is well dispersed in the slurry. High strength in the green bodies is important, especially when casting larger pieces. As mentioned previously the binder also provides additional steric hindrance and is a crucial component to keeping the viscosity low.

5.3.2 Fracture surface morphology and microstructure

The micrographs of the green bodies in Figure 4-13 and Figure 4-14 give an indication of the arrangement of the particles in the binder matrix. The particles were arranged tightly in the binder matrix which is beneficial for sintering and increases the green strength of the pieces. The size of the SiC particles was 1 μm on average, but the size distribution was quite large. The pores that were not due to trapped air in the slurry were in the 1 μm range which is small enough to be removed by sintering. [29] The larger pores due to the trapped air in the slurry will remain during sintering as defects.

The dispersed carbon additives could not be distinguished with much certainty though it is possible that these smaller particles are transported toward the surface of the green bodies along with the water. The surface of the plaster moulds would always be covered with a layer of fine black powder after casting SiC-CB green bodies. The same observation could not be done with SiC-Novolac as the yellow Novolac powder does not provide a sufficient contrast to the plaster. This type of segregation phenomena has been described by others when using bimodal particle distribution. [59]

5.3.3 Thermal behaviour

The thermal behaviour of the SiC-CB green body sample was as expected. There was an initial mass loss of 3.2 wt. % at 400 °C due to the binder burning out and the evaporation of moisture. Then the mass was mostly constant until the temperature reached 1250 °C. At this temperature, the SiO_2 present in the material can begin to decompose or be reduced. [71]

The TGA of the SiC-Novolac green sample also had the binder burnout at 400 °C but the mass loss was higher due to additional pyrolysis of Novolac. The total mass loss below 650

°C was 6 wt. % so half of that could be attributed to Novolac when comparing with SiC-CB. The initial Novolac content was 7 wt. % and the expected carbon yield was 45 % (from Figure 4-5) so the carbon content after pyrolysis was ~3 wt. %. There was an increase of 1.5 wt. % in mass from 650 to 1200 °C that was followed by a sharp decrease. This was most likely due to oxidation of SiC during the measurement. Carbon black could be a more effective guard against oxidation than Novolac leading to this difference in behaviour. The mass loss at higher temperatures (> 1200 °C) indicates that the SiO2 is removed again and it is unknown whether these fluctuations will impact sintering.

5.3.4 Density and density gradients

The density of the green bodies was expected to increase with increased solid loading, though that was not the case. The highest average green body density was achieved for 75 wt. % solid loading for SiC-CB and 72 wt. % for SiC-Novolac. This could be explained by increased viscosity leading to more air being trapped in the slurry, or by the reduced freedom of the particles to pack densely while settling.

The density of the green bodies varied with the position in the sample, typically with the bottom section having the highest density. This can be explained by the settling of the particles after casting leading to higher packing. A related explanation could be that the foam trapped in the slurry was more present in the middle and top as it migrated upwards. In some cases, the density gradient was less pronounced for higher solid loadings. This would again relate to the reduced freedom of particles to settle densely, reducing the overall density and the density gradient.

5.4 Sintered body characterisation

The sintered body characterisations provided some insight into the effect carbon black and Novolac had on the material. There were differences throughout the analysis that are important to qualify for continued development.

5.4.1 Density and linear shrinkage

The densities of the sintered samples all reached over 92 % TD, but the densities were higher for SiC-CB, in some cases reaching as high as 98 %. This indicates that the samples at least reached the intermediate stage of sintering. The difference between SiC-CB and SiC-Novolac

can be attributed to the already lower green densities in SiC-Novolac due to the effects discussed previously. In addition, the sintering temperature was slightly lower for SiC-Novolac so the grain growth that characterises the final stage of sintering may not have occurred.

The density variation depending on the position in the bar observed in the green bodies was also preserved in the sintered bodies. This inhomogeneity, though slight, could lead to internal stresses in the material. In larger products, the differences could be quite large and in the worst-case lead to fracture at stresses lower than the theoretical fracture stress.

The linear shrinkage was, as expected reduced by increased green body density. The shrinkage was more pronounced in the SiC-Novolac samples than the SiC-CB samples even at high green body densities. This could be due to the pyrolysis of the Novolac resulting in a higher change in volume. To keep the linear shrinkage under 20 % carbon black would be a better carbon source.

5.4.2 Porosity, fracture surface and failure analysis

The fracture surfaces of the sintered samples differed quite a lot depending on the carbon source. The SiC-CB sample was characterised by a large degree of transgranular fracture while SiC-Novolac had evidence of more intergranular fracture mechanisms. Both materials had some evidence of tearing open and pulling out as well, though this was more pronounced in SiC-Novolac.

The nature of the SiC-Novolac fracture surface could be an indication of higher fracture toughness. On the other hand, is has been described in several studies that carbon can deposit on the grain boundaries and in fact reduce the fracture toughness by forming weaknesses in the grain boundaries. Skarpeid compared the fracture toughness of SiC sintered with carbon black and resin as carbon sources and concluded the fracture toughness was indeed lower in samples sintered with resin. [72]

The porosity observed in the materials was in part due to air trapped in the slurry and could not be removed by sintering. Porosity determined by image analysis of the polished surfaces could be slightly exaggerated due to the polishing step possibly mechanically ripping out material around the pores, making them appear larger. The pores on the fracture surfaces were much smaller and fewer in numbers.

5.4.3 Phase composition and polytypic transitions

The XRD-diagrams showed that the sintered samples had other polytypes present compared to their respective raw powder, notably 2H and 4H-SiC. Only trace amounts of the 2H polytype was measured so the samples were mainly composed of 4H and 6H, a fair assumption to make for phase calculations. The approximate phase composition of the sintered samples calculated by Rietveld fitting in Topas revealed the fraction of 4H-SiC was higher in the carbon black sample. This could be due to the higher sintering temperature inducing the 6H → 4H polytypic phase transition. [73]

A higher ratio of 4H to 6H polytype can lead to anisotropic grain growth. [74]The anisotropy of the 4H polytype can increase the fracture toughness by crack deflection or crack bridging. [75] Grain anisotropy could not be determined from the fracture surface micrographs despite the differences in fracture mechanisms. However, the intergranular fracture in SiC-Novolac indicates the grain boundaries are weaker than the grains. This could be related to the increased fraction of 4H though other parameters could be affecting the fracture toughness.

The presence of graphite in the sintered samples can be attributed to the graphitisation of the carbon additives. The graphitisation of carbon black can occur for temperatures between 1000 and 3000 °C [76] and Novolac may graphitize when heated beyond the pyrolysis temperature. [77] Some have suggested that the presence of excess carbon and graphite specifically on the grain boundaries can impact the strength and decrease fracture toughness. [72] An argument can be made that excess Novolac will form a glassy carbon phase and finally graphite on the particle surface. This would decrease the intergranular strength and the fracture toughness and led to the intergranular fracture observed in this study.

6 Conclusion

Different aspects of slip casting SiC with additives for solid-state pressureless sintering have been studied from the consolidation step to the final dense bodies. The effect of dispersant concentration, solid loading and pH on slurry rheology was determined and different characteristics of the green and sintered bodies were studied. In addition, the differences between carbon black and Novolac as sintering additives were established. The main findings are summarised as follows:

- SiC-CB reached minimum viscosity with the addition of 0.5 wt. % Hypermer KD7 and pH adjusted to 9. The maximum solid loading was 76 wt. %.
- SiC-Novolac reached minimum viscosity with the addition of 1.5 wt. % Hypermer KD7 and the pH should be kept close to 8. The maximum solid loading was 74 wt. %.
- The dissolution of Novolac at high pH is an important factor in the viscosity of the slurry and high pH values increase viscosity.
- High-quality green bodies were cast with the main difficulty being foam removal. Surface defects appeared with increased solid loading and viscosity.
- Inhomogeneities in density were discovered in all the samples due to sedimentation after casting. High slurry viscosity can impede tight packing and decrease green body density so increased solid loading did not lead to increased green body density.
- The highest sintered density (~98 % TD) was achieved in the SiC-CB samples with 75 wt. % solid loading. SiC-Novolac had lower density overall.
- Linear shrinkage was decreased with increased green body density. Linear shrinkage was higher in SiC-Novolac samples.
- There were some differences in phase composition and fracture mechanism between SiC-CB and SiC-Novolac sintered samples. It was suggested this was due to different sintering temperatures and carbon concentrations.

7 Further work

The findings in this thesis can be built on further to optimize the slip casting by decreasing viscosity. Tailoring the dispersant concentration based on the specific surface area of the powders could help normalize these findings. The choice of dispersant or combinations of dispersants was not covered and could be an interesting factor to optimize depending on the carbon source. Another aspect could be tailoring the particle size distribution and the particle shape to maximize solid loading while lowering viscosity. Bimodal size distribution and spherical particles have the potential for higher packing densities [59]

The distribution of carbon throughout the green bodies can impact the sintering, thus, studying the elemental composition throughout a slip cast body would be interesting. One approach could be the use of X-ray photoelectron spectroscopy (XPS), which has high detection limits [78] and can give the uniformity of elemental composition across a surface.

8 Bibliography

1. Choi, B., B. Liu, and J.-W. Jeong, *Effects of hydrothermal aging on SiC-DPF with metal oxide ash and alkali metals.* Journal of Industrial and Engineering Chemistry, 2009. **15**(5): p. 707-715.
2. Eddy, C. and D. Gaskill, *Silicon Carbide as a Platform for Power Electronics.* Science, 2009. **324**(5933): p. 1398-1400.
3. Kuzin, V.V., S.Y. Fedorov, and S.N. Grigor'ev, *Technological Provision of the Quality of Ring Edges of Silicon-Carbide Friction Couples for the End Seals of the Pumps.* Refractories and Industrial Ceramics, 2018. **58**(6): p. 647-651.
4. Pachaiyappan, R., R. Gopinath, and S. Gopalakannan, *Processing Techniques of a Silicon Carbide Heat Exchanger and its Capable Properties – A Review.* Applied Mechanics and Materials, 2015. **787-787**(Alternative Energy Sources, Materials and Technologies): p. 513-517.
5. Rajan, N., et al., *Fabrication and testing of micromachined silicon carbide and nickel fuel atomizers for gas turbine engines.* Microelectromechanical Systems, Journal of, 1999. **8**(3): p. 251-257.
6. Chawla, K.K., *Ceramic matrix composites*. 1993, London: Chapman & Hall.
7. Prochazka, S., *Sintering of Silicon Carbide*, in *Mass Transport Phenomena in Ceramics*, A.R. Cooper and A.H. Heuer, Editors. 1975, Springer US: Boston, MA. p. 421-431.
8. Raju, K. and D.-H. Yoon, *Sintering additives for SiC based on the reactivity: A review.* Ceramics International, 2016. **42**(16): p. 17947-17962.
9. Saint-Gobain. *Technical Ceramics*. 2018 [cited 2018 24 June]; Available from: https://www.refractories.saint-gobain.com/hexoloy/technical-ceramics.
10. Datta, M.S., A.K. Bandyopadhyay, and B. Chaudhuri, *Sintering of nano crystalline α silicon carbide by doping with boron carbide.* Bulletin of Materials Science, 2002. **25**(3): p. 181-189.
11. Tanaka, H., et al., *Influence of silica and aluminum contents on sintering of and grain growth in 6H-SiC powders.* Journal of the American Ceramic Society, 2000. **83**(1): p. 226-228.
12. Lee, J.-H., et al., *Dispersion stability and its effect on tape casting of solvent-based SiC slurries*. Vol. 10. 2009. 301-307.
13. Li, W., et al., *Effect of TMAH on rheological behavior of SiC aqueous suspension.* Journal of the European Ceramic Society, 2004. **24**(14): p. 3679-3684.
14. Rao, R., H.N. Roopa, and T.S. Kannan, *Effect of pH on the Dispersability of SiC Powders in Aqueous Media*. Vol. 25. 1999. 223-230.
15. Sun, J. and L. Gao, *Dispersing SiC powder and improving its rheological behaviour.* Journal of the European Ceramic Society, 2001. **21**(13): p. 2447-2451.

16. Wang, F., et al., *Effect of organic additives on mechanical properties of SiC ceramics prepared by a modified gelcasting method.* Processing and Application of Ceramics, 2016. **10**(4): p. 227-233.

17. Diaz-Cano, A., R.W. Trice, and J.P. Youngblood, *Stabilization of highly-loaded boron carbide aqueous suspensions.* Ceramics International, 2017. **43**(12): p. 8572-8578.

18. Li, S., et al., *Surface modification and characterization of carbon black by sodium lignosulphonate.* Surface and Interface Analysis, 2017. **49**(3): p. 197-204.

19. Liu, H., et al., *Charging behavior of carbon black in a low-permittivity medium based on acid-base charging theory.* Journal of Materials Chemistry C, 2015. **3**(16): p. 3980-3988.

20. Contarini, S., et al., *XPS study on the dispersion of carbon additives in silicon carbide powders.* Applied surface science, 1991. **51**(3-4): p. 177-183.

21. Sun, L., et al., *Dispersion Properties of a Water-Soluble Phenol-Formaldehyde Resin.* Journal of Dispersion Science and Technology, 2009. **30**(5): p. 605-608.

22. Britannica, T.E.o.E. *Silicon carbide*. Encyclopædia Britannica, 2008.

23. Weimer, A.W., *Carbide, nitride and boride materials synthesis and processing*. 1997, London: Chapman & Hall.

24. Pierson, H.O., *Handbook of Refractory Carbides & Nitrides : Properties, Characteristics, Processing and Applications*. Handbook of Refractory Carbides & Nitrides : Properties, Characteristics, Processing and Apps. 1996, Burlington: Elsevier Science.

25. Kanzaki, M. *Crystal structure data for VESTA*. [cited 2017 12 December].

26. Matovic, B. and T. Yano, *Silicon Carbide and Other Carbides*. 2013. 225-244.

27. McGinnis, M., Grahl, C. L., *The evolution of SiC kiln furniture.* Ceramic Industry, 2000. **150**(11): p. C6-C11.

28. Rahaman, M.N., *Sintering of ceramics*. 2008, Boca Raton, Fla: CRC Press.

29. Fang, Z.Z., *Thermodynamics of sintering*. 2010, Oxford, England :. 3-32.

30. Richerson, D.W., *Modern ceramic engineering : properties, processing, and use in design*. 3rd ed. ed. Materials engineering. Vol. 29. 2006, Boca Raton, Fla: CRC Press.

31. McColm, I.J. and N.J. Clark, *Forming, shaping and working of high-performance ceramics*. 1988, Glasgow: Blackie.

32. Prochazka, S., *Hot pressed silicon carbide*. 1974, Google Patents.

33. Clegg, W.J., *Role of Carbon in the Sintering of Boron-Doped Silicon Carbide.* Journal of the American Ceramic Society, 2000. **83**(5): p. 1039-1043.

34. Greskovich, C. and J.H. Rosolowski, *Sintering of Covalent Solids.* Journal of the American Ceramic Society, 1976. **59**(7-8): p. 336-343.

35. Gross, E., D.B. Dahan, and W.D. Kaplan, *The role of carbon and SiO2 in solid-state sintering of SiC.* Journal of the European Ceramic Society, 2015. **35**(7): p. 2001-2005.

36. Magnani, G., G. Sico, and A. Brentari, *Two-Step Pressureless Sintering of Silicon Carbide-Based Materials.* Advances in Science and Technology, 2014. **89**: p. 70-75.

37. Group, R. *Sanitary Ware Plant*. 2018 [cited 2018 27 June]; Available from: http://www.roca.com/memoria_roca_2014/industrial_management.html.

38. Lange, F.F., *Powder Processing Science and Technology for Increased Reliability.* Journal of the American Ceramic Society, 1989. **72**(1): p. 3-15.

39. Santiso, E. and E. Muller, *Dense packing of binary and polydisperse hard spheres.* Mol. Phys., 2002. **100**(15): p. 2461-2469.

40. Hiemenz, P.C. and R. Rajagopalan, *Principles of colloid and surface chemistry*. 3rd ed., rev. and expanded. ed. 1997, New York: Marcel Dekker.

41. Lombardo, D., et al., *Soft Interaction in Liposome Nanocarriers for Therapeutic Drug Delivery.* Nanomaterials, 2016. **6**(7): p. 125.

42. Hashiba, M., et al., *The zeta-potential measurement for concentrated aqueous suspension by improved electrophoretic mass transport apparatus — application to Al 2 O 3 , ZrO 3 and SiC suspensions.* Journal of Materials Science, 1988. **23**(8): p. 2893-2896.

43. Varga, I., F. Csempesz, and G. Záray, *Effect of pH of aqueous ceramic suspensions on colloidal stability and precision of analytical measurements using slurry nebulization inductively coupled plasma atomic emission spectrometry.* Spectrochimica Acta Part B: Atomic Spectroscopy, 1996. **51**(2): p. 253-259.

44. ICBA, *Carbon Black User's Guide*. 2016.

45. Figueiredo, J.L. and M.F.R. Pereira, *The role of surface chemistry in catalysis with carbons.* Catalysis Today, 2010. **150**(1): p. 2-7.

46. Xu, R., C. Wu, and H. Xu, *Particle size and zeta potential of carbon black in liquid media.* Carbon, 2007. **45**(14): p. 2806-2809.

47. Yasin, S. and P.F. Luckham, *Investigating the effectiveness of PEO/PPO based copolymers as dispersing agents for graphitic carbon black aqueous dispersions.* Colloids and Surfaces A: Physicochemical and Engineering Aspects, 2012. **404**(Supplement C): p. 25-35.

48. Lu, K.T., et al., *The Acid-Catalyzed Phenol–Formaldehyde Reaction: Critical Runaway Conditions and Stability Criterion.* Process Safety and Environmental Protection, 2004. **82**(1): p. 37-47.

49. Plenco. *Phenolic Novolac and Resol Resins*. [cited 2018 22. February]; Available from: https://plenco.com/phenolic-novolac-resol-resins.htm.

50. Shih, H.Y. and A. Reiser, *A Percolation View of Novolak Dissolution. 4. Mechanism of Inhibitor Action.* Macromolecules, 1995. **28**(16): p. 5595-5600.

51. Reiser, A., et al., *Novolak–diazonaphthoquinone resists: The central role of phenolic strings.* Journal of Vacuum Science & Technology B: Microelectronics and Nanometer Structures, 2000. **18**(3): p. 1288-1293.

52. Ellefsen, O.M., *Stabilization of dispersions of carbon additives used for sintering of SiC*, in *Department of Materials Science and Engineering*. 2017, NTNU: Trondheim.

53. Nojiri, M., et al., *Analysis of Anionic Polymer Dispersant Behavior in Dense Silicon Nitride and Carbide Suspensions Using an AFM.* Journal of Nanoparticle Research, 2001. **3**(2): p. 237-244.

54. Mezger, T.G., *The rheology handbook : for users of rotational and oscillatory rheometers*. 3rd rev. ed. ed. European coatings tech files. 2011, Hannover: Vincentz.

55. Mewis, J. and N.J. Wagner, *Colloidal suspension rheology*. 2012, Cambridge University Press: Cambridge ;,New York.

56. Mueller, S., E.W. Llewellin, and H.M. Mader, *The rheology of suspensions of solid particles.* Proceedings of the Royal Society A: Mathematical, Physical and Engineering Science, 2010. **466**(2116): p. 1201-1228.

57. Shi, F.N. and T.J. Napier-Munn, *A model for slurry rheology.* International Journal of Mineral Processing, 1996. **47**(1): p. 103-123.

58. Mooney, M., *The viscosity of a concentrated suspension of spherical particles.* Journal of Colloid Science, 1951. **6**(2): p. 162-170.

59. Ferreira, J.M.F. and H.M.M. Diz, *Effect of Solids Loading on Slip-Casting Performance of Silicon Carbide Slurries.* Journal of the American Ceramic Society, 1999. **82**(8): p. 1993-2000.

60. Vol'fson, R.E., et al., *Slip-cast corundum bars.* Refractories, 1976. **17**(7): p. 410-413.

61. Verba, L.I. and É.V. Degtyareva, *Rheological and technological properties of titanium dioxide slips and the properties of the castings.* Refractories, 1978. **19**(3): p. 158-163.

62. Smith, P.A., *Microstructural characterization of alumina and silicon carbide slip-cast cakes.* Journal of the American Ceramic Society, 1996. **79**(10): p. 2515-2526.

63. Makarenkova, R.G., *The influence of a high polymer on some properties of fused-quartz slips and castings.* Refractories, 1976. **17**(5): p. 312-315.

64. Chou, K.S. and L.J. Lee, *Effect of Dispersants on the Rheological Properties and Slip Casting of Concentrated Alumina Slurry.* Journal of the American Ceramic Society, 1989. **72**(9): p. 1622-1627.

65. Hirata, Y., S. Yamada, and Y. Fukushige, *Colloidal processing of silicon carbide.* Materials Letters, 1993. **16**(5): p. 295-299.

66. Pivinskii, Y. and V. Bevz, *Preparation and rheological, technological, and binding properties of aqueous zircon suspensions.* Refractories, 1979. **20**(7): p. 490-496.

67. Rutman, D., et al., *Influence of structural characteristics of alumina on the properties of aqueous suspensions and castings made from them.* Refractories, 1980. **21**(3): p. 168-173.

68. Keefe, K., *Pyrolysis of Phenolic Resin in SiC*, in *Kazuo Inamori School of Engineering*. 2015, Alfred University: Alfred, New York, USA. p. 61.

69. Miller-Chou, B.A. and J.L. Koenig, *A review of polymer dissolution.* Progress in Polymer Science, 2003. **28**(8): p. 1223-1270.

70. Shih, H.-Y. and A. Reiser, *A Percolation View of Novolak Dissolution. 4. Mechanism of Inhibitor Action.* Macromolecules, 1995. **28**(16): p. 5595-5600.

71. Stobierski, L. and A. Gubernat, *Sintering of silicon carbideI. Effect of carbon.* Ceramics International, 2003. **29**(3): p. 287-292.

72. Skarpeid, H., *The effect of carbon and boron carbide additions in pressure assisted sintered silicon carbide*, in *Department of Materials Science and Engineering*. 2017, Norwegian University of Science and Technology: Trondheim. p. 102.

73. Yoshimura, H.N., et al., *Sintering of 6H(α)-SiC and 3C(β)-SiC powders with B4C and C additives.* Journal of Materials Science, 2002. **37**(8): p. 1541-1546.

74. Lee, J.-K., et al., *Effect of starting phase on microstructure and fracture toughness of hot-pressed silicon carbide.* Materials Letters, 2002. **57**(1): p. 203-208.

75. Young-Wook, K., M. Mamoru, and H. Hideki, *Grain Growth and Fracture Toughness of Fine-Grained Silicon Carbide Ceramics.* Journal of the American Ceramic Society, 1995. **78**(11): p. 3145-3148.

76. Schaeffer, W.D., W.R. Smith, and M.H. Polley, *Structure and Properties of Carbon Black - Changes Induced by Heat Treatment.* Industrial & Engineering Chemistry, 1953. **45**(8): p. 1721-1725.

77. Oberlin, A., *Carbonization and graphitization.* Carbon, 1984. **22**(6): p. 521-541.

78. G., S.A., *Detection limits in XPS for more than 6000 binary systems using Al and Mg Kα X-rays.* Surface and Interface Analysis, 2014. **46**(3): p. 175-185.

9 Appendix

A. Slurries for viscosity measurements

Table 9-1 List of all slurries prepared for viscosity measurements with the different combinations of powder composition, solid loading, dispersant concentration and pH

Name	SiC system	Solid loading [wt. %]	Dispersant concentration [wt. %]	pH
SiCNovo72_0.50	SiC-Novolac	72	0.50	9
SiCNovo72_0.75	SiC-Novolac	72	0.75	9
SiCNovo72_1.00	SiC-Novolac	72	1.00	9
SiCNovo72_1.25	SiC-Novolac	72	1.25	9
SiCNovo72_1.40	SiC-Novolac	72	1.40	9
SiCNovo72_1.50	SiC-Novolac	72	1.50	9
SiCNovo72_1.60	SiC-Novolac	72	1.60	9
SiCNovo72_1.75	SiC-Novolac	72	1.75	9
SiCNovo73_1.50	SiC-Novolac	73	1.50	9
SiCNovo74_1.50	SiC-Novolac	74	1.50	9
SiCNovo75_1.50	SiC-Novolac	75	1.50	9
SiCNovo72_1.50_pH8	SiC-Novolac	72	1.50	8.2
SiCNovo_1.50_pH8.6	SiC-Novolac	72	1.50	8.6
SiCNovo_1.50_pH9	SiC-Novolac	72	1.50	9.0
SiCNovo_1.50_pH9.5	SiC-Novolac	72	1.50	9.5
SiCNovo_1.50_pH10	SiC-Novolac	72	1.50	9.9
SiCCB72_0.10	SiC-CB	72	0.10	9
SiCCB72_0.20	SiC-CB	72	0.20	9
SiCCB72_0.30	SiC-CB	72	0.30	9
SiCCB72_0.40	SiC-CB	72	0.40	9
SiCCB72_0.50	SiC-CB	72	0.50	9
SiCCB72_0.60	SiC-CB	72	0.60	9
SiCCB72_0.70	SiC-CB	72	0.70	9
SiCCB72_1.00	SiC-CB	72	1.00	9
SiCCB74_0.50	SiC-CB	74	0.50	9
SiCCB75_0.50	SiC-CB	75	0.50	9
SiCCB76_0.50	SiC-CB	76	0.50	9
SiCCB77_0.50	SiC-CB	77	0.50	9
SiCCB78_0.50	SiC-CB	78	0.50	9

SiCCB72_0.50_pH8.1	SiC-CB	72	0.50	8.1
SiCCB72_0.50_pH8.6	SiC-CB	72	0.50	8.6
SiCCB72_0.50_pH9.1	SiC-CB	72	0.50	9.1
SiCCB72_0.50_pH9.9	SiC-CB	72	0.50	9.9

B. SiC-CB and SiC-Novolac slurry viscosity and fitting parameters for the Herschel-Bulkley model

The measured viscosities of the slurries at shear rate 40s-1 are listed in Table 9-2 along with the yield stress, the consistency index and the flow index that characterise a Herschel-Bulkley fluid.

Table 9-2 Measured viscosity at shear rate 40 s^{-1} and calculated fitting paramters for the Herschel-Bulkley model for each slurry studied.

Name	**η [cP]**	**HB model fitting parameters**		
	at 40 s^{-1}	**τ_o [Pa]**	**K**	**n**
SiCNovo72_0.50	641	0.48	14.41	0.20
SiCNovo72_0.75	452	0.52	5.86	0.30
SiCNovo72_1.00	354	0.47	3.93	0.34
SiCNovo72_1.25	306	0.44	3.14	0.36
SiCNovo72_1.40	276	0.43	0.42	0.40
SiCNovo72_1.50	273	0.38	1.70	0.43
SiCNovo72_1.60	367	0.42	2.92	0.43
SiCNovo72_1.75	405	0.30	3.00	0.46
SiCNovo73_1.50	297	0.28	2.65	0.40
SiCNovo74_1.50	402	0.29	3.62	0.40
SiCNovo75_1.50	501	0.41	5.01	0.37
SiCNovo72_1.50_pH8	176	0.43	1.58	0.38
SiCNovo_1.50_pH8.6	204	0.39	2.01	0.35
SiCNovo_1.50_pH9	273	0.47	2.64	0.37
SiCNovo_1.50_pH9.5	276	0.43	0.42	0.40
SiCNovo_1.50_pH10	251	0.49	2.60	0.35
SiCCB72_0.10	248	0.43	3.30	0.29
SiCCB72_0.20	198	0.34	2.35	0.28
SiCCB72_0.30	183	0.55	2.34	0.29
SiCCB72_0.40	163	0.48	1.37	0.33
SiCCB72_0.50	137	0.52	1.63	0.30

SiCCB72_0.60	139	0.65	1.46	0.33
SiCCB72_0.70	177	0.40	2.08	0.32
SiCCB72_1.00	193	0.39	2.01	0.35
SiCCB74_0.50	226	0.39	2.98	0.29
SiCCB75_0.50	250	0.42	3.02	0.32
SiCCB76_0.50	340	0.47	4.93	0.27
SiCCB77_0.50	654	0.46	7.14	0.35
SiCCB78_0.50	838	0.47	1.,50	0.22
SiCCB72_0.50_pH8.1	152	0.43	1.58	0.38
SiCCB72_0.50_pH8.6	141	0.47	1.43	0.35
SiCCB72_0.50_pH9.1	137	0.52	1.63	0.31
SiCCB72_0.50_pH9.9	136	0.46	1.57	0.33

The parameters K and n of the Herschel-Bulkley model given in equation (9.1) were calculated by using the polyfit function in Matlab (version R2017b) with a linear regression of equation (9.2). n is the slope and ln(K) is the intercept.

$$\tau = \tau_o + K\dot{\gamma}^n \tag{9.1}$$

$$\ln(\tau - \tau_o) = lnK + n * ln\dot{\gamma} \tag{9.2}$$

C. Calculation of theoretical density of powders and sintered bodies

The density of the powders can be calculated using the rule of mixtures. The densities of the carbon sources given by the manufacturer. The density of SiC and B_4C is the theoretical density based on crystal structure.

Table 9-3 Calculated powder densities from the rule of mixtures

Material	Density [g/cm^3]
SiC	3.21
B_4C	2.52
Carbon black	1.90
Novolac	1.24
SiC-CB	3.1656
SiC-Novolac	3.0772

D. Conversion table between mass fraction and volume fraction for the powders

This table gives the volume fraction of powder in a slurry corresponding to the different solid loadings and powders used. The conversion uses the powder mix densities calculated and presented in Table 9-3.

Table 9-4 Conversion table for calculating volume fraction in the SiC slurries for different solid loadings given in weight percent.

Solid loading [wt. %]	Volume fraction	
	SiC-CB	SiC-Novolac
72	0.448	0.455
73	0.461	0.468
74	0.473	0.480
75	0.487	0.494
76	0.500	0.507
77	0.514	0.521
78	0.528	0.535

E. Green body density results

The green body density of the samples is presented in Table 9-5. The error is calculated from the standard deviation in the measurements. Each measurement was taken 5 times.

Table 9-5 Green body density of the samples measured geometrically

Sample	Solid loading [wt. %]	Position	GB density [g/cm^3]	± [g/cm^3]
SiC-CB 01	72	Bottom	1.5861	0.0651
SiC-CB 02	75	Bottom	1.6122	0.0445
SiC-CB 03	75	Bottom	1.7591	0.0446
SiC-CB 03	75	Middle	1.7455	0.0292
SiC-CB 03	75	Top	1.6999	0.0586
SiC-CB 03	75	Bottom	1.7660	0.0871
SiC-CB 03	75	Top	1.7507	0.0652
SiC-CB 04	76	Bottom	1.7256	0.0696
SiC-CB 04	76	Middle	1.6674	0.1091
SiC-CB 04	76	Top	1.6463	0.0848
SiC-CB 05	76	Bottom	1.5863	0.0542
SiC-CB 05	76	Middle	1.5902	0.0981
SiC-CB 05	76	Top	1.5736	0.0575
SiC-Novolac 01	72	Bottom	1.5677	0.0580
SiC-Novolac 01	72	Bottom	1.5697	0.0926
SiC-Novolac 01	72	Middle	1.5274	0.0767
SiC-Novolac 01	72	Top	1.5312	0.1007
SiC-Novolac 02	74	Bottom	1.5940	0.0401
SiC-Novolac 02	74	Middle	1.5842	0.0401
SiC-Novolac 02	74	Top	1.4647	0.0444
SiC-Novolac 03	74	Bottom	1.4097	0.1312
SiC-Novolac 03	74	Middle	1.4469	0.0334
SiC-Novolac 03	74	Top	1.4739	0.0666
SiC-Novolac 04	74	Bottom	1.4090	0.0959
SiC-Novolac 04	74	Middle	1.4442	0.1258
SiC-Novolac 04	74	Top	1.4335	0.0592

F. Sintered density and linear shrinkage results

The sintered densities measured by the Archimedes principle are listed in Table 9-6 along with the open and closed porosities. The theoretical density used for the calculating closed porosity was 3.1656 g/cm^3. Table 9-7 gives the linear shrinkage of the sintered samples relative to the green samples.

Table 9-6 Measured densities of sintered samples. Measurements by Archimedes method with isopropanol as the immersion fluid.

Sample	Solid loading [wt. %]	Position	Bulk density [g/cm^3]	Apparent porosity [%]	Closed porosity [%]
SiC-CB 01	72	Bottom	2.9403	1.4575	5.6590
SiC-CB 03	75	Bottom	3.0952	0.4291	2.2239
SiC-CB 03	75	Middle	3.0897	0.5213	2.3961
SiC-CB 03	75	Top	3.0748	1.3503	2.8675
SiC-CB 05	76	Bottom	2.9983	0.7247	5.2838
SiC-CB 05	76	Middle	2.9970	0.7245	5.3270
SiC-CB 05	76	Top	3.0044	0.4692	5.0914
SiC-Novolac 02	74	Bottom	2.9152	2.5588	7.9090
SiC-Novolac 02	74	Middle	2.9591	1.1235	6.5240
SiC-Novolac 02	74	Top	2.9233	2.2883	7.6552

Table 9-7 Linear shrinkage is the sintered samples in h measured geometrically.

Sample	Linear shrinkage in h [%]
SiC-CB 01	18.44
SiC-CB 03	19.46
SiC-CB 03	17.71
SiC-CB 03	18.15
SiC-CB 05	19.89
SiC-CB 05	18.68
SiC-CB 05	18.64
SiC-Novolac 02	21.77
SiC-Novolac 02	21.50
SiC-Novolac 02	22.45

G. Image analysis of porosity by ImageJ

The greyscale histograms of the SEM images and the thresholds used for porosity determination by image analysis in ImageJ are presented in Figure 9-1. The despeckle function was used to reduce noise.

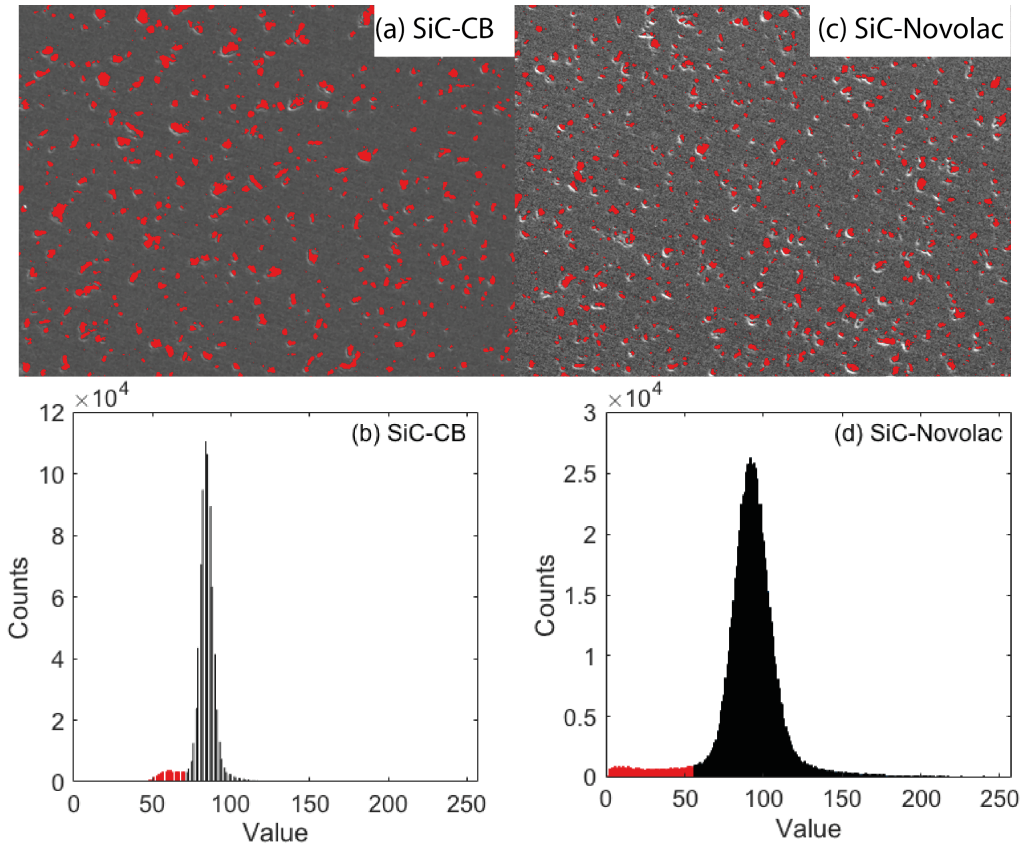

Figure 9-1 Thresholds used for image analysis of porosity with their corresponding SEM micrographs. The images were analysed in ImageJ. The red areas represent porosity.